Available online at www.sciencedirect.com
SCIENCE DIRECT®
Journal of volcanology and geothermal research
ELSEVIER
Journal of Volcanology and Geothermal Research 129 (2004) 37–60
www.elsevier.com/locate/jvolgeores

Dynamics of bubble oscillation and wave propagation in viscoelastic liquids

Mie Ichihara [a,*], Hiroshi Ohkunitani [b], Yoshiaki Ida [c], Masaharu Kameda [b]

[a] *Center for Northeast Asian Studies, Tohoku University, Kawauchi, Aoba-ku, Sendai 980-8576, Japan*
[b] *Department of Mechanical Systems Engineering, Tokyo Noko University, Koganei, Tokyo 184-8588, Japan*
[c] *Graduate School and Faculty of Science, Himeji Institute of Technology Shosha, Himeji 671-2201, Japan*

Received 3 July 2002; received in revised form 1 December 2002; accepted 28 January 2003

Abstract

Decrease of the velocity of a pressure wave in magma by the presence of bubbles is regarded as a fundamental process in seismoacoustic activities of a volcano. However, we show that the large viscosity of magma ($\geq 10^5$ Pa s) prevents this decrease in wave velocity. To investigate how the acoustic properties of a liquid–bubble mixture depend on liquid rheology, laboratory experiments were conducted using silicone oil and syrup. Both liquids have a viscosity as high as 1000 Pa s. Propagation of a pressure wave and the radial motion of a bubble were observed in a shock-tube-type apparatus, but were quite different in the two liquids. Although the velocity of the pressure wave significantly decreased as the void fraction in silicone oil did, bubbles did not decrease the wave velocity in syrup. From conducting several material tests, we found that both liquids are viscoelastic, and that the rigidity (the shear elasticity) of silicone oil is smaller than that of the syrup by several orders. The motion of a single bubble and propagation of the pressure wave were calculated using the Oldroyd model for linear viscoelasticity. The numerical solutions explained the difference as a result of the different rigidities of the two liquids. The same mathematical model was then applied to understand pressure wave propagation in bubbly magmas with a variety of viscosities. Results of the experiments and the subsequent numerical analyses suggest that pressure wave propagation in a liquid–bubble mixture and the motion of a single bubble depend significantly on the viscoelastic properties of the liquid. The sound velocities of liquids with large viscosities and rigidities are not decreased by bubbles; magmas with high viscosity are in this category. To evaluate propagation velocity and attenuation of a pressure wave in a bubbly liquid, we need to deal with the dispersion relationship with an adequate liquid rheology model. The present results give an insight into the bubble dynamics in a viscoelastic liquid, which is important for developing mathematical and experimental methods to investigate seismoacoustic phenomena in volcanoes.

Keywords: pressure wave; bubble; viscoelasticity; magmas; experimental studies; dynamic property of a mixture

1. Introduction

Magma is frequently a mixture of liquid, bub-

* Tel./Fax: +81-22-217-6272.
E-mail address: mie@cneas.tohoku.ac.jp (M. Ichihara).

0377-0273/03/$ – see front matter © 2003 Elsevier B.V. All rights reserved.
doi:10.1016/S0377-0273(03)00231-2

bles, and solid particles. When we work on the seismoacoustic activities of a volcano, we are almost certainly confronted with acoustic phenomena problems. In fact, many features of volcanic activities are ascribed to the presence of bubbles in magma. Bubbles can significantly reduce the sound velocity of magma (Kiefer, 1977) and may generate spectral features of long-period earthquakes, tremors, and acoustic waves in the atmosphere (e.g. Chouet, 1996; Benoit and McNutt, 1997; Garces and McNutt, 1997; Kumagai and Chouet, 2001). The motion of a huge bubble in the volcanic conduit can generate seismic waves (Vergniolle and Brandeis, 1996; Ripepe and Gordeev, 1999), and oscillation or bursting of bubbles at the magma surface can generate acoustic waves in the air (Vergniolle and Brandeis, 1994, 1996; Ripepe et al., 1996).

A considerable number of works have been published, mainly in the engineering area, on the dynamics of a single bubble, and on pressure waves in a bubbly liquid. Radial motion of a single bubble was first formulated by Rayleigh (1917) for an incompressible Newtonian liquid. When motion of the bubble is very fast, radiation of energy as a pressure wave into the liquid becomes important. Such an effect was included into the equation by taking account of liquid compressibility (Keller and Miksis, 1980; Prosperetti and Lezzi, 1986). Effects of heat transfer (Prosperetti, 1991) and mass transfer (e.g. Takemura and Matsumoto, 1994) between the liquid and the bubble were also formulated and investigated. The equations were tested by laboratory experiments and good agreements obtained (e.g. Shima, 1997; Kameda and Matsumoto, 1999). These equations for a single bubble were applied to formulate the acoustic properties of a liquid–bubble mixture (Prosperetti, 1984; Caflish et al., 1985; Commander and Prosperetti, 1989). The acoustic properties were also formulated based on scattering theory, which is often used for composite solid materials (Gaunaurd and Überall, 1981; Varadan et al., 1985). A decrease of the wave velocity, dispersion and attenuation represented by these equations agree well with the laboratory experiments (e.g. Silberman, 1957; Cheyne et al., 1995; Commander and Prosperetti, 1989). A numerical method that reproduces the measured waveform of a shock wave in a bubbly liquid has been presented (Kameda et al., 1998).

However, all the above studies are intended for liquids with low viscosity. An important feature of a magmatic system is the huge variety of the viscosity, which can be less than 1 Pa s, but can also be more than 10^{14} Pa s, and the viscoelasticity with a relaxation time from 10^{-11} to 10^{4} s (Webb and Dingwell, 1995). Such a large variety of viscosities has not been treated in the engineering area. Although we can find several theoretical and numerical works on bubble dynamics in various viscoelastic models (e.g. Fogler and Goddard, 1970, 1971; Tanasawa and Yang, 1970; Brujan, 1999), the effects of the elasticity and viscosity have yet to be systematically investigated. Only a few experiments using highly viscous or viscoelastic liquids have been reported. Brujan et al. (1996) observed the behavior of laser-induced cavitation bubbles in polymer solutions that have non-Newtonian shear-thinning viscosity. They recognized an obvious effect of the non-Newtonian rheology of the liquids only when a bubble collapsed very close to a solid boundary. However, the viscosity of the liquids used in their experiment was still small, 0.01 Pa s.

Although currently theories and models of bubble dynamics developed for low-viscosity liquids are applied to volcanic systems, their applicability has not been tested. Possible effects of the high viscosity and viscoelasticity have been discussed by several authors. Mikada (1992) pointed out that sound velocity of magma with high viscosity might not be effectively decreased by bubbles because a volumetric change of the bubbles is difficult. In such a case, models that assume a low sound velocity for the magma do not work. Bubbles may increase the effective viscosity of the mixture (Manga and Loewenberg, 2001), causing large attenuations of pressure waves (Garces et al., 2000). When magma is excited at periods smaller than the relaxation time, the melt's behavior is more akin to a solid than to a liquid, and viscous attenuation may decrease (Garces et al., 2000). Viscous magma around a bubble is expected to exhibit non-Newtonian viscoelastic behavior in explosive events and to go into fragmen-

tation (Dingwell and Webb, 1989). These possibilities need quantitative evaluation.

Recently, experiments investigating the dynamic behaviors of bubbly liquids with high-viscosity and/or viscoelasticity have begun to be conducted in the area of volcanology. Bagdassarov and Dingwell (1993) measured the dynamic shear modulus of a high-viscosity magma ($10^{9.5}$–$10^{11.5}$ Pa s) with void fraction of 0–0.3 using the forced torsion oscillation (0.005–10 Hz). Llewellin et al. (2002) applied the same technique for a viscous syrup (40–70 Pa s) with void fractions of 0–0.46. Both experiments demonstrated the viscoelastic nature of the mixtures. Lane et al. (2001) conducted a scaled experiment simulating gas–liquid flow in a volcanic conduit. They used a gum rosin–organic solvent solution, which simulates the rheology of hydrated magma (Phillips et al., 1995). They produced various types of two-phase flows, from bubbly flow to fragmented foam flow, and demonstrated that pressure oscillations of different characteristics occurred in different flow regimes. Although their experiment included lots of similarities to actual volcanic processes, formulations to describe the complicated phenomena have not yet been established.

In the present study, we conducted experiments using two liquids: a high-viscosity silicone oil (Shin-Etsu KF96H-1M, density 978 kg/m^3) and a commercial syrup (density 1400 kg/m^3). The viscosity of both liquids was about 1000 Pa s, which is comparable to that of relatively viscous basaltic magma. Liquids with such a large viscosity have never been used in experiments on bubble dynamics. We investigated the responses of a bubble and of liquid–bubble mixtures to weak shock waves. A shock wave was used for three reasons. Firstly, a stepwise pressure increase is one of the simplest mathematical functions. Secondly, propagation of a shock wave in bubbly magma is relevant in explosive volcanic phenomena such as explosion earthquakes (Nishimura and Chouet, 2002) and phreatomagmatic explosions (Zimanowski et al., 1991). Thirdly, the phenomena have been well studied and understood in cases of low-viscosity liquids (Campbell and Pitcher, 1958; Noordzij and van Wijngaarden, 1974; Kameda et al., 1998).

A shock wave behaves quite differently in the two test liquids despite similar viscosities and void fractions. The behavior of a single bubble is also quite different in the two liquids. We ascribe the differences to the different elastic properties of the liquids. Mathematical models that adequately describe the motion of a single bubble and the wave propagation are explored.

Our experimental conditions are quite simple in contrast to actual volcanic systems. The major purpose of the experiments is to establish the fundamental theory. We regard it as the essential step to develop scaling laws for the two-phase phenomena, which are a useful mathematical tool for volcanology. The present experimental results, clearly demonstrating the effects of not only viscosity but also elasticity, give new insights into bubble dynamics in a viscoelastic liquid.

Several material tests are also conducted in order to confirm the different elastic properties of the liquids. The results are qualitatively consistent with the theories used to explain the bubble motion and the wave propagation. However, quantitative comparisons are limited, because the common methods cannot measure the viscoelastic properties in the present ranges of parameters and time. In order to complete our understanding of the bubble dynamics in viscoelastic liquids, we need to develop techniques to measure time-dependent material properties in wider ranges.

2. Experimental apparatus and methods

2.1. Shock tube

Fig. 1 shows a sketch of the experimental apparatus. Experiments were conducted using a vertical shock tube made of Pyrex glass having an inner diameter of 52 mm and a total length of about 2.8–3.4 m. The shock tube consists of three parts: atmospheric-pressure liquid (LQ), atmospheric-pressure air (A-P), and high-pressure air (H-P). The H-P part is initially kept at 150 kPa and separated from the lower parts by a plastic diaphragm. A shock wave is generated by an electrical rupturing of the diaphragm.

The test section in the liquid part is made from

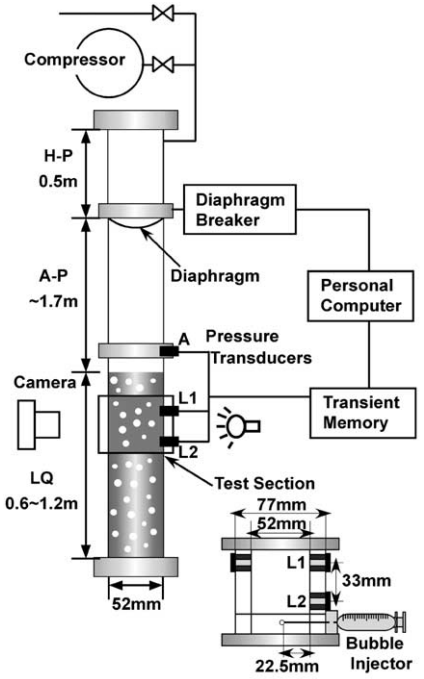

Fig. 1. A vertical shock tube consisting of atmospheric-pressure liquid (LQ), atmospheric-pressure air (A-P), and high-pressure air (H-P) parts. A detailed sketch of the test section and the bubble injector are shown at bottom right.

a hollow acrylic rectangular block (77 mm × 90 mm) designed to reduce optical distortion. Minimum and maximum wall thicknesses are 12.5 and 33.2 mm, respectively. Photographs are taken with rear illumination.

Pressure is measured by piezoelectric transducers (Kistler-603B, rise time 1 μs, resonant frequency 400 kHz; PCB-113A21, rise time 1 μs, resonant frequency 500 kHz). The transducers are connected to charge amplifiers as prescribed by the manufacturers (Kistler-5011A; PCB-402A16). The signals are stored in a personal computer through a digital transient memory (Autonics, APC-204). The sampling rate is 1 MHz. The transducers are flush-mounted on the side-wall of the tube at A in the air and at L1 and L2 in the test section. The transducers have been calibrated by the manufacturers. We also checked that all three transducers record the same shock-wave amplitude in the shock tube without liquid (Fig. 4a).

2.2. Pressure wave experiments

When liquid was poured into the shock tube, the surrounding air was automatically mixed into the liquid to form bubbles. The pouring height and the rate were manually controlled so that bubbles were uniformly distributed in the liquid.

In the experiments with the silicone oil, void fraction and bubble size distribution could be modified after the LQ part was filled with the liquid–bubble mixture in the following way. The mixture was pressurized at 150–200 kPa for about 10 min and released. Under compression, a certain amount of air in the bubbles dissolved into the liquid. Completely dissolved bubbles did not exsolve when the mixture was brought back to the atmospheric pressure. Because smaller bubbles are more likely to dissolve due to surface tension, the size distribution of the remaining bubbles became more uniform after this procedure. According to the material report provided by the manufacturer, the solubility of air in the silicone oil is 20 vol% at atmospheric pressure. The liquid was not in equilibrium with the bubbles in the experiments and bubbles grew or shrank in minutes. Because this time scale, which is controlled by diffusion of the air in the liquid, is much longer than the time scale of one experiment (ms), the diffusion effect on the experimental results is regarded as being unimportant. The solubility of air in the syrup seems much smaller than that of the silicone oil, though precise details of it are not known; thus this method was not effective for the syrup.

The test section was photographed just before each experiment (Fig. 2). Void fraction (ϕ) for each experiment was determined by measuring radii of all bubbles in a certain part of the test section (Fig. 2, inside the green frame). Bubble radii were measured by fitting circles (red circles in Fig. 2) to the bubbles one by one. For the examples in Fig. 2, we obtained (a) $\phi = 0.0116$ and (b) $\phi = 0.0113$. Because the resolution of the digital images is 0.07 mm/pixel, the measurement error due to uncertainty of the bubble edge is ± 0.035 mm. With consideration of the error, ranges of the void fractions for the cases in Fig. 2 are (a) 0.0085–0.0135 and (b) 0.01–0.0128, respectively.

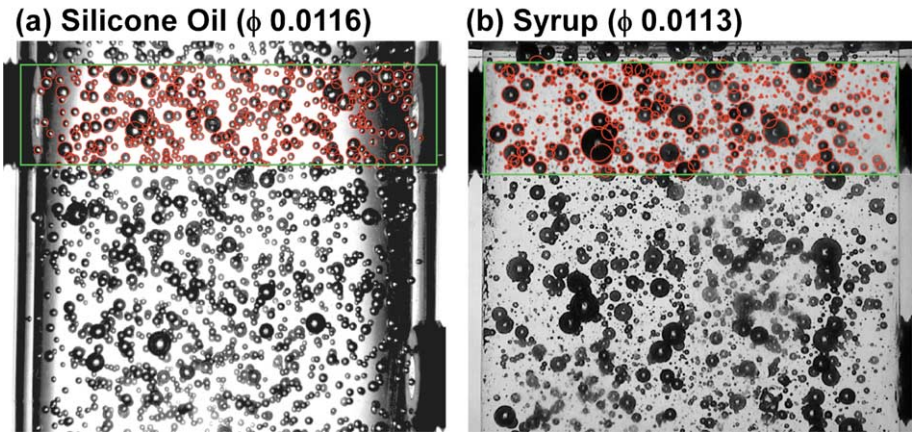

Fig. 2. Images of the test section taken just before the incidence of the pressure waves. All the bubbles recognized in the green frame have been fitted with circles. By measuring the radii of the circles, the void fractions were determined as (a) 0.0116 (0.0085–0.0135) and (b) 0.0113 (0.01–0.0128). The uncertainty is due to the image resolution (0.07 mm/pixels).

Since it took almost a day to analyze just one image utilizing the precise method above, we applied a quick method for most experiments. Using this method, we recorded positions of three arbitrary points on the edge of each bubble on the image coordinate. Then the radius of a circle passing through the three points was calculated. Differences between the void fractions obtained by the precise method and the quick method were smaller than the possible error due to image resolution. For example, in the case of Fig. 2a, we obtained 0.0101 by the quick method as against 0.0116 by the precise one. In another case, we obtained 0.0042 and 0.0038 by the quick and the precise methods, respectively.

Because acrylic is a relatively flexible material, wave propagation inside the test section may be affected by deformation of the wall. Velocity c of a pressure wave in a circular tube is represented by:

$$c = \frac{c_o}{\sqrt{1 + f(x)\rho c_o^2/E}} \tag{1}$$

$$f(x) = \frac{1 - \nu + (1+\nu)(1+x)^2}{x(1+x/2)} \tag{2}$$

where c_o and ρ are the sound velocity and the density of the liquid (or mixture) in the tube, respectively, E and ν are the Young modulus and the Poisson ratio of the tube material, respectively, and x is the wall thickness divided by the inner radius (Matsuo et al., 1997). Using $E = 3$ GPa, $\nu = 0.3$ and $0.48 < x < 1.28$ for the test section, we find that 5.0×10^8 Pa $< E/f(x) < 8.5 \times 10^8$ Pa. When $\rho c_o^2 \geq E/f(x)$, namely, when the sound velocity c_o is larger than several hundreds m/s, the actual value is not measured. In fact, Eq. 1 is applicable to long waves, because it is based on an assumption of static deformation, which is axi-symmetric and uniform along the tube axis. For a short wave such as the shock-wave front, the effect of wall deformation may be smaller. Nevertheless, the effect should be taken into consideration in these conditions. In order to reduce such an effect, pressure was measured in a brass tube ($E = 100$ GPa, $\nu = 0.35$, $x = 0.54$) in some experiments. The acrylic tube was inserted 200 mm below the brass section, and the void fraction was measured there.

2.3. The single-bubble experiments

We attempted to investigate motion of a single bubble in the absence of other surrounding bubbles.

To remove bubbles from the silicone oil in the LQ part, we pressurized the mixture at 150–200 kPa until all bubbles dissolved into the liquid.

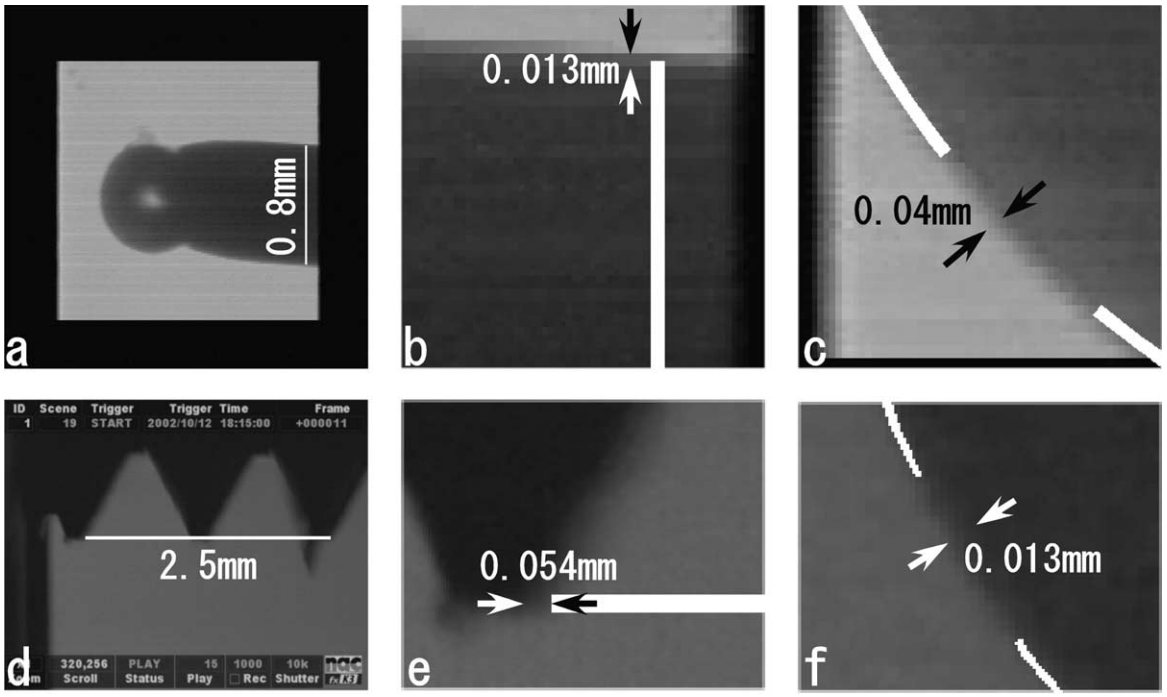

Fig. 3. Images taken by the high-speed video camera in the single-bubble experiments in silicone oil (panels a–c) and in syrup (panels d–f). The uncertainty of the edges is indicated by arrows. (a) The needle of the bubble injector is used as a scale. (b) A magnified view of panel a. (c) A magnified view of a bubble (radius 1.1 mm). (d) The sensor holder is used as a scale. (e) A magnified view of panel d. (f) A magnified view of a bubble (radius 0.65 mm).

Next, an injector was inserted from a small hole beneath the test section (Fig. 1) and air was injected. The size of the bubble was adjusted by moving the injector piston. After making a bubble, the injector was removed and the hole was closed with a screw. When the bubble rose to the same level as one of the transducers in the test section, the experiment was started. The bubble motion was observed using a high-speed digital video camera (Photoron FASTCAM-Ultima-UV) at a rate of 13 500 frames per second (fps). The image resolution of the camera with that frame rate was 128×128 pixels. The images were at once recorded on S-VHS tape, and transferred to a computer for analyses. The bubble radius was measured on each frame by the methods described above. The needle of the injector was photographed in advance with the same camera setting in order to be used as a scale (Fig. 3a).

In the example presented in Fig. 3a–c, measurement errors due to uncertainties regarding the edges are 0.013 and 0.04 mm for the needle (outer diameter 0.8 mm) and for the bubble (radius 1.11 mm), respectively.

For the syrup, we decreased viscosity by warming the liquid above 90°C and let the bubbles go. Experiments were conducted with a void fraction smaller than 0.004. One bubble, isolated from the others and located at a level of one of the transducers, was chosen. The bubble motion was taken by a high-speed digital video camera (nac MEMRICAM-K3) at a rate of 4000 fps with 640×256 pixels. The images were recorded on mini-DV tape, and analyzed on a computer. The transducer holder was used as a scale (Fig. 3d). An example is presented in Fig. 3d–f; measurement errors are 0.054 mm for the 2.5 mm scaler and 0.013 mm for the bubble (radius 0.65 mm).

3. Experimental results and preliminary analyses

3.1. Pressure wave in bubbly liquids

A shock wave generated in the apparatus without liquid was measured by the pressure transducers A, L1, and L2 as presented in Fig. 1. All three transducers recorded the same shock-wave amplitude (Fig. 4a), indicating that they were adequately calibrated.

Using the same set of transducers, pressure waves were measured in silicone oil with various void fractions (ϕ). Results for $\phi \sim 0$, 0.009, and 0.018 are presented in Fig. 4b–d. In each figure, the numbers indicating the individual lines represent distances (mm) measured from the liquid surface, positive downward. Two shock waves are recorded at A: the first step up to $\sim$20 kPa is the incident shock wave going downward, and the second one to $\sim$40 kPa is its reflection from the liquid surface. The origin of the horizontal axis is set at the time when the first pressure perturbation is recognized on the pressure profile at L1.

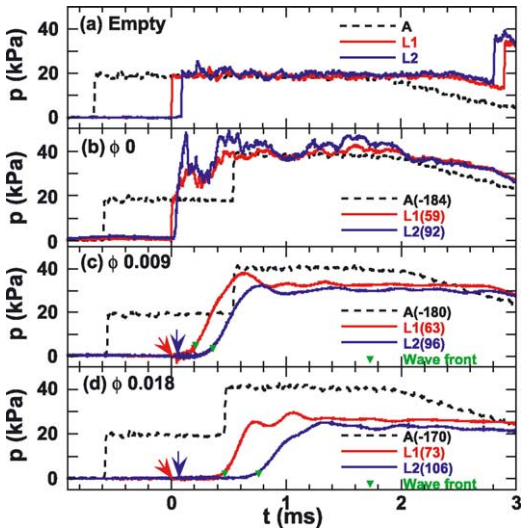

Fig. 4. Pressure waves in the empty shock tube (a), in silicone oil with void fractions of 0 (a), 0.009 (b), and 0.018 (c), respectively. The broken black line, the red line, and the blue line are the data taken at A, L1, and L2 in the shock tube (Fig. 1), respectively. The numbers indicating the lines are distances of the transducers in mm measured from the liquid surface, positive downward. In panels c and d, the precursor signal on each profile is indicated by an arrow of the same color. The points at which the pressure increases by 10% of the maximum value on each profile are indicated by green triangles. The wave velocity is calculated using the time interval between the triangles.

In Fig. 4b with few bubbles, the sharp shock front propagates into the liquid. The propagation velocity of the wave front is 868 m/s. The reflection wave from the bottom arrives at $t \sim 2$ ms. Pressure oscillation in a similar time scale is caused by wave reflections between the bottom and the surface of the liquid column. Fluctuations at higher frequencies right after the shock front are considered to be due to the non-flat liquid surface, remaining small bubbles, and oscillation of the tube wall.

As the void fraction increases (Fig. 4c,d), the wave front becomes smoother, and the propagation velocity and the amplitude decrease. The waveform, consisting of the smooth front followed by oscillation, is similar to a typical shock wave in a low-viscosity liquid containing bubbles (Noordzij and van Wijngaarden, 1974). A weak precursor is recognized ahead of the main step, as indicated by arrows. The velocity of the precursor is more than 900 m/s. The green triangles in Fig. 4c,d indicate the points at which pressure increases by 10% of the maximum value on each profile.

Using the time interval between these points, wave velocities were calculated as 212 m/s for $\phi = 0.009$ (Fig. 4c), and 113 m/s for $\phi = 0.018$ (Fig. 4d). Matsumoto and Kameda (1996) measured wave velocity in the same way in a bubbly liquid with low viscosity. Their results were in good agreement with the theoretical shock-wave velocity in a liquid with a small fraction of bubbles and without dissipation (Campbell and Pitcher, 1958):

$$c_m = \sqrt{\frac{p_0 + \Delta p}{\rho \phi (1-\phi)}} \tag{3}$$

where c_m is the velocity of the shock-wave front, p_0 is the initial pressure, Δp is the shock-wave amplitude, and ρ is the density of the liquid. For the cases in Fig. 4c,d, $c_m = 124$ m/s ($\phi = 0.009$, $\Delta p = 3.5 \times 10^4$ Pa) and $c_m = 84$ m/s ($\phi = 0.018$, $\Delta p = 2.5 \times 10^4$ Pa). The measured wave velocities (212 m/s in Fig. 4c, 113 m/s in Fig. 4d) are larger than those given by Eq. 3.

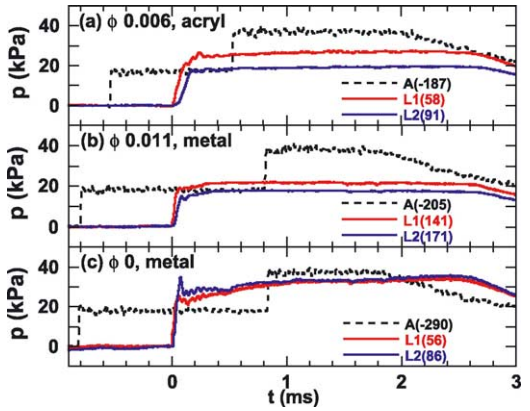

Fig. 5. Pressure waves in syrup with void fractions of 0.006 (a), 0.011 (b), and 0 (c). The acrylic test section was used for panel a and the brass test section was used for panels b and c. The numbers indicating the lines are distances of the transducers in mm measured from the liquid surface, positive downward.

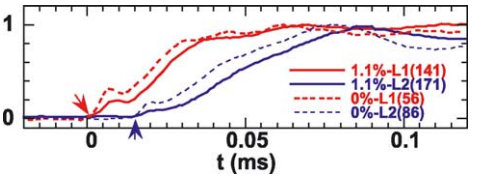

Fig. 6. The wave profiles in syrup with void fractions of 0.011 (Fig. 5c) and 0 (Fig. 5d) are compared with the amplitude normalized to unity. Onsets of the waves are indicated by arrows.

To obtain these values from Eq. 3, we need $\phi = 0.003$ and 0.01, respectively. These values are too small compared with the observation even if we take account of the measurement error. It is also noted that the present analysis tends to underestimate the wave velocity, because the wave front becomes smoother as it propagates.

A pressure wave in syrup with $\phi = 0.006$ is presented in Fig. 5a. The wave velocity is obviously much larger (650 m/s using the 10% points), and the wave front is steeper than the waves in silicone oil. Separation between the precursor and the main wave front is not clear in the syrup. Because of the large wave velocity, deformation of the acrylic tube cannot be ignored. We conducted experiments with the brass tube, and obtained a wave velocity as large as 1620 m/s with a void fraction of $\phi = 0.011$ (Fig. 5b). Although the amplitude of the wave decreases significantly as it propagates, the wave front is as steep as that in the bubble-free liquid (Fig. 5c). If the waveforms in Fig. 5b,c with the normalized amplitudes (Fig. 6) are compared, that the red and the blue pairs of lines have identical slopes, except for the initial

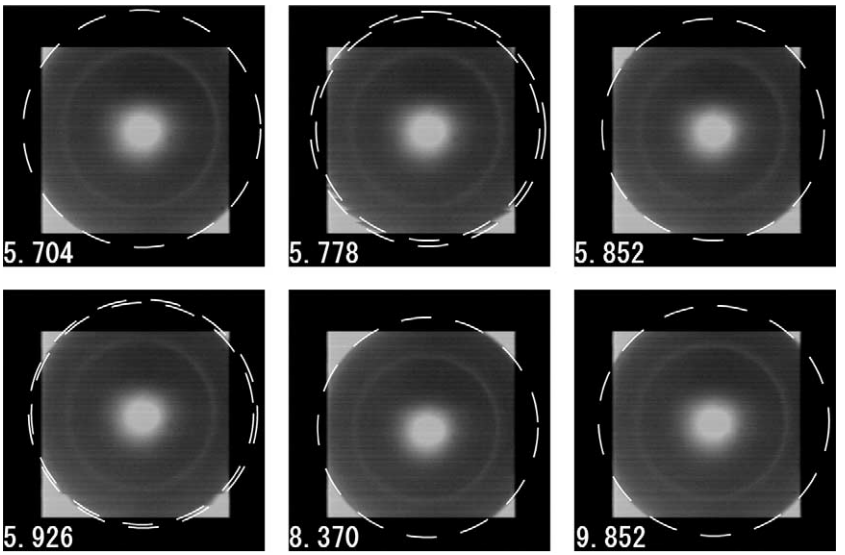

Fig. 7. Images of a single bubble in silicone oil. The broken circle indicates the bubble surface.

small steps indicated by arrows, can be seen. These steps propagate at the same velocity (2000 m/s) in both cases and can be regarded as corresponding to the precursor in the silicone oil. Without bubbles, the main phase propagates as fast as the precursor, and faster than in the case with bubbles.

3.2. Motion of a single bubble

Because it is acknowledged that the pressure wave in a bubbly liquid is controlled by volumetric changes of individual bubbles (van Wijngaarden, 1972), we investigated the motion of a single bubble in those liquids. The results are presented below.

Selected frames of the video records of the motion of a single bubble in silicone oil are presented in Fig. 7. The images were taken with the same scale as Fig. 3a–c. The bubble surface is fitted by a broken circle. We can see that the spherical shape of the bubble is maintained during its motion. On the images at times 5.778 and 5.926 ms, the bubble motion is so fast that two different radii are recognized on a single frame. We measured both and took their average as the radius at each of those times. The initial radius was 1.105 ± 0.025 mm.

Changes of bubble radius in silicone oil and syrup are plotted in Fig. 8a,b, respectively. In Fig. 8a, the closed circles connected with dotted lines represent data obtained by the quick measurement. The accuracy of the measurement is supported by the open circles obtained independently by the precise method. The solid lines display pressure changes measured by a transducer at the same level as the bubble. It can be seen, at a glance, that bubble behavior is quite different between the two liquids.

Two phases are distinguished in the bubble in Fig. 8a: a rapid decrease in the radius followed by a more gradual decrease. Rapid oscillation is superimposed on the second phase. We infer that the rapid and the slow shrinkage regimes are exposures of the elastic and viscous responses of the bubble, respectively.

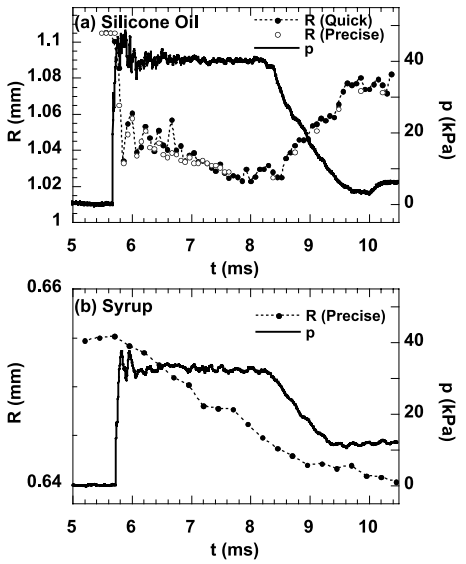

Fig. 8. Results of the single-bubble experiment (a) in silicone oil, and (b) in syrup. The points represent changes of the bubble radius and the solid line represents pressure changes measured at the same level as the bubble. The bubble radius was measured by precise and quick methods for panel a (see the text for details). The results are shown by the closed and open circles, which agree well with each other.

4. Viscoelastic properties of the liquids

We applied several rheology tests to the test liquids. It is noted that there is no established method to measure the dynamic properties of liquids in the time scale of the present experiment (0.1–1 ms), though some new methods are under development (Yoneda, 1998, 2000; Kajitani et al., 2002).

The measured properties are summarized in Table 1. The important results obtained by the rheology tests are:

(1) Both the silicone oil and the syrup have viscoelastic properties.

(2) While the viscosities of the liquids are similar, the rigidity of the silicone oil is three orders smaller than that of the syrup.

The methods to obtain these values are explained below.

4.1. Long-term responses

The slow response of the silicone oil was mea-

sured by static and dynamic tests using a rotational stress rheometer (Rheometric Scientific, SR-200). The rheometer applies a given torsion stress to the specimen inserted between two plates (25 mm diameter, 1.4 mm gap) and measures the strain.

In the static test, a fixed torsion stress is applied to the specimen (for 30 s in the present case) and then removed. From the strain rate under torsion stress and recovery after stress release, viscosity (η_s) and rigidity (μ_s) are calculated (Graessley, 1993). Applying a torsion stress of 100 Pa, we obtained $\eta_s = 960$ Pa s and $\mu_s = 8.2$ kPa, respectively. Viscosity tended to decrease and rigidity to increase as the stress and strain rate increased. For 1000 Pa, we obtained $\eta_s = 930$ Pa s and $\mu_s = 9.3$ kPa, respectively.

For the dynamic test, a sinusoidal torsion stress is applied. By measuring the amplitude and the phase delay of the associated strain, we obtain the complex shear modulus as a function of angular frequency ω. The test was done for the available frequency range of the apparatus, and the result is presented in Fig. 9 with open circles and squares. The solid and broken lines and triangles in the figure are described later. The frequency dependence of the complex modulus is similar to that of a typical polymeric viscoelastic liquid in the viscous frequency domain (Graessley, 1993). The real part, $G'(\omega)$, and the imaginary part, $G''(\omega)$, represent the elastic and viscous responses of the material, respectively. They are linked to μ_s and η_s in their low-frequency limit as $\lim_{\omega\to 0} G'(\omega)/\omega^2 = \eta_s^2/\mu_s$ and $\lim_{\omega\to 0} G''(\omega)/\omega = \eta_s$, respectively (Graessley, 1993). From the data presented in Fig. 9, we obtained $\eta_s = 960$ Pa s and $\mu_s = 8.3$ kPa, respectively, which are consistent with the results of the static test.

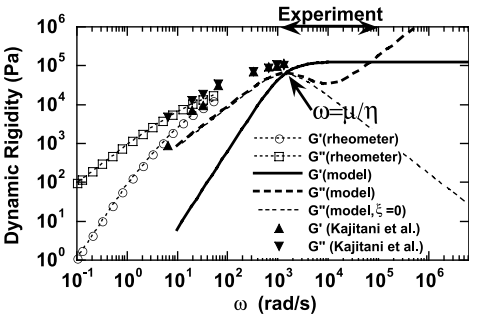

Fig. 9. The dynamic rigidity of silicone oil is shown as a function of angular frequency ω. The real and the imaginary parts of the dynamic rigidity are denoted by $G'(\omega)$ and $G''(\omega)$, respectively. The open symbols are the data measured by a stress rheometer. The lines are the model employed in the numerical analyses with the parameters listed in Table 1. The time range of the present experiment is indicated on the upper horizontal axis. The triangles are presented by Kajitani et al. (2002) based on their observation of bubble oscillation.

We tried the same tests on the syrup. However, the syrup protruded out of the plates and measurements were unstable. Viscosity of the syrup was measured by a rotational viscometer. It had the value of 850 Pa s right after it was taken out of the container. When the syrup was heated to 90°C to remove bubbles, and then cooled to room temperature (21°C), its viscosity increased to 1150 Pa s. We consider that this viscosity increase is due to the loss of water.

Table 1
Mechanical properties of the silicone oil (Shin-Etsu KF96-1M) and the syrup used in the model and measured by the mechanical tests

	Silicone oil			Syrup			Magma
	Model	Measured	Method	Model	Measured	Method	Model
μ (MPa)	0.12	0.22–3.9	Ultrasound	700	700–960	Ultrasound	10^4
η (Pa s)	84	960	Rheometer	1150	1150	Viscometer	10^{0-14}
ξ (Pa s)	1.68	–		0	–		0
K (GPa)	1	1	Ultrasound	8	8	Ultrasound	20
ρ (kg/m^3)	980	980	Catalog	1400	1400	Measured	2600
K_g (MPa)	0.1	0.1	Atmosperic-p	0.1	0.1	Atmospheric-p	1

Representative values for magma are also listed.

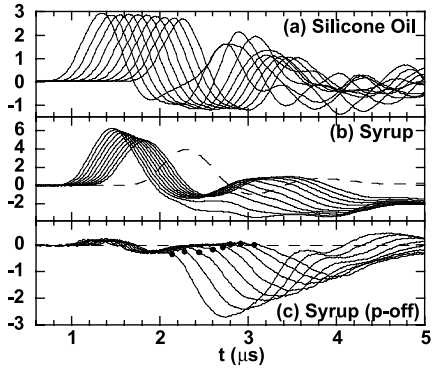

Fig. 10. Signals taken by the receiver transducer in the ultrasonic tests. (a) Data in silicone oil for source–receiver distances from 0.1 to 1 mm with an interval of 0.1 mm. (b) Data in syrup for source–receiver distances from 1.5 to 2.4 mm with an interval of 0.1 mm. The broken line is for the distance of 3.5 mm. (c) The broken line is subtracted from each profile in panel b so that the first positive phases (the p-wave) are canceled. The points indicate the onset of the second negative phases (the s-wave).

4.2. Short-term responses

In order to observe the short-term behaviors of the liquids, ultrasonic tests were conducted.

A pair of piezoelectric s-wave transducers (Panametrics V153, 1 MHz) were used in transmission mode at various spacings, and the velocities of the p-wave and s-wave (denoted by c_p and c_s) were determined from the transfer time of the acoustic wave.

The bulk modulus, K, and the rigidity, μ, of the liquids are calculated using the relation, $c_p = \sqrt{(K + \frac{4}{3}\mu)/\rho}$ and $c_s = \sqrt{\mu/\rho}$, respectively (Webb and Dingwell, 1995).

Fig. 10 shows the output of the receiver transducer. In silicone oil, the distance between the transducers (L) was changed from 0.05 to 1.4 mm, and data taken every 0.05 mm. Fig. 10a shows the data from $L = 0.1$ mm to $L = 1.0$ mm with an interval of 0.1 mm. In syrup, L was changed from 0.5 to 3.5 mm, and data taken with intervals of 0.25 or 0.1 mm. Fig. 10b presents the data from $L = 1.5$ mm to $L = 2.4$ mm with an interval of 0.1 mm (solid lines) and the data for $L = 3.5$ mm (broken line). The first positive phase, seen in both liquids, is regarded as the p-wave. Although the transducers are designed for an s-wave, slightly non-parallel alignment of the transducers produces a p-wave signal. The propagation velocities are determined as 1000 m/s in the silicone oil and 2500 m/s in the syrup. In Fig. 10a, the equally spaced initial phases start to be entangled around $t = 2$ μs. This is ascribed to the arrival of the reflected p-wave, because the disturbance propagates with an apparent velocity of $\sim 1000/3$ m/s and has the same polarity as the first one. The s-wave is not distinguished in the wave field. On the other hand, in Fig. 10b, the different phase after the first wave peaks has the opposite polarity from the first phase. We regard this as the s-wave. When the broken line is subtracted from the other wave profiles, with the time and the amplitude adjusted so that the p-wave phase is canceled, the second phase becomes clearer (Fig. 10c). Onsets of the second phase are marked with solid circles. The propagation velocity was determined as 710 m/s. The corresponding rigidity is $\mu_\infty = 700$ MPa.

Yoneda (personal communication, 2002) measured rigidity of these liquids by the reflection method. He put the liquids on a buffer rod attached to an s-wave transducer (Panametrics, V220-BA-RM, 5 MHz). An s-wave was generated by the transducer, and as the wave reflected from the interface between the rod and the liquid, it was measured by the same transducer. The ratio of the reflected s-wave amplitude to the incident s-wave amplitude is:

$$R_{ol} = A_o \frac{\rho c_s - \rho_o c_{so}}{\rho c_s + \rho_o c_{so}} \tag{4}$$

where quantities for the rod are indicated with a subscript 'o', and A_o is the attenuation factor of the system. By measuring the reflectivity of the rod–air interface (R_{oa}), A_o is determined as $R_{oa} = -A_o$. The rod is made of fused silica with $\rho_o = 2200$ kg/m^3 and $c_{so} = 3760$ m/s. Using the known densities of the liquids, the s-wave velocities of the silicone oil and the syrup were determined as 39 ± 24 m/s and 826 m/s, respectively. The corresponding rigidities are 0.22–3.9 MPa and 960 MPa, respectively. The accuracy of the data for the silicone oil is limited, because the difference between R_{ol} and R_{oa} is very small.

5. Numerical calculation

5.1. Single bubble behavior

We now show that different bubble behaviors can be ascribed to different rigidities.

We employ the equation of motion for a spherical bubble in an incompressible liquid with linear viscoelasticity (Fogler and Goddard, 1970). It is acknowledged for low-viscosity liquids that liquid compressibility is unimportant when the bubble wall velocity is much smaller than the sound velocity of the liquid (Prosperetti and Lezzi, 1986). The effect of liquid compressibility on bubble oscillation in viscoelastic liquids has not been sufficiently investigated, and needs to be the subject of further investigation.

The equation presented by Fogler and Goddard (1970) is:

$$R\ddot{R}+\frac{3}{2}\dot{R}^2=\frac{1}{\rho}\left(p_g-\int_\infty^R\frac{3\tau_{rr}}{r}dr-\frac{2\sigma_s}{R}-p-p_o\right) \quad (5)$$

$$\tau_{rr}=-2\int_0^t N(t-t')\dot{\varepsilon}_{rr}dt' \quad (6)$$

where R is the bubble radius, r is the distance from the center of the bubble, t is the time, σ_s is the surface tension, p and p_o are the acoustic and the static pressures in the liquid, respectively, p_g is the pressure in the bubble, τ_{rr} and ε_{rr} are the radial components of deviatoric stress and strain rate tensors, respectively, and $N(t)$ is a memory function for a relaxation modulus. The integral term in Eq. 5 is transformed as:

$$\int_\infty^R\frac{3\tau_{rr}}{r}dr=12\int_0^t N(t-t')\frac{R^2(t')\dot{R}(t')\ln[R(t')/R(t)]}{R^3(t')-R^3(t)}dt' \quad (7)$$

In Eq. 7, the following relations required by the continuity and incompressibility of the liquid were used:

$$u_r=\frac{\dot{R}R^2}{r^2} \quad (8)$$

$$(r')^3=r^3+R^3(t')-R^3(t) \quad (9)$$

where r' denotes the position at past time t' $(0\le t'\le t)$ of a particle which is at position r at the present time t.

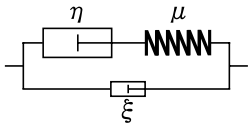

Fig. 11. Schematic diagram of the linear Oldroyd model.

From the bubble behavior in the silicone oil, we infer that the liquid first deforms elastically and then relaxes viscously. In order to represent such a property, we employ the linear Oldroyd model (Tanasawa and Yang, 1970; Fogler and Goddard, 1971), which consists of one elastic component and two viscous components, as schematically shown in Fig. 11. The model is equivalent to the Jeffreys model (Barnes et al., 1989). The corresponding memory function is:

$$N(t)=\xi\delta(t)+\mu\exp(-t/\tau) \quad (10)$$

$$\tau=\eta/\mu \quad (11)$$

where μ represents the elasticity, τ the relaxation time, and η and ξ the viscosity. The model includes the Maxwell viscoelastic model as a case with $\xi=0$. It also includes the Newtonian liquid as a case in which $\xi=0$ and $\mu\to\infty$ with $\eta=\mu\tau$ fixed.

Substituting Eq. 10 into Eq. 7, one obtains:

$$\int_\infty^R\frac{3\tau_{rr}}{r}dr=4\xi\frac{\dot{R}}{R}+12\mu\int_0^t\exp\left(-\frac{t-t'}{\tau}\right)\frac{R^2(t')\dot{R}(t')\ln[R(t')/R(t)]}{R^3(t')-R^3(t)}dt' \quad (12)$$

Eq. 5 with Eq. 12 were solved numerically by the fourth order Runge–Kutta method. The surface tension was neglected. Integration in Eq. 7 was calculated with the trapezoid method in the range $t-15\tau<t'<t$, and the contribution of the integral outside this range was negligible. The ambient pressure p at each time step was given by interpolation of the experimental data. The pressure inside the bubble, p_g, was calculated assuming an isotropic process:

$$p_gR^{3\gamma}=p_{go}R_o^{3\gamma} \quad (13)$$

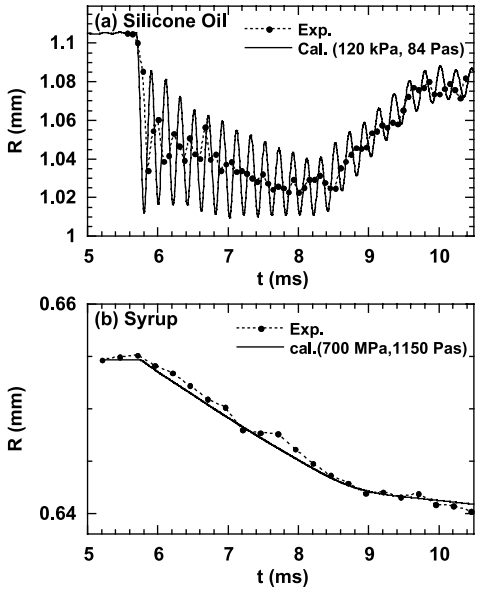

Fig. 12. Numerical solutions for the bubble radius with Maxwell viscoelastic model (Oldroyd model with $\xi = 0$). The conditions correspond to the experiments shown in Fig. 8. (a) For silicone oil, the rigidity and viscosity are chosen so that the solution fits the experimental data. (b) For syrup, the rigidity and viscosity measured by the material tests are used in the calculation.

where the subscript 'o' indicates the initial values at time zero and is the ratio of specific heats of the air. The initial conditions are $R = R_o$ and $\dot{R} = 0$.

First, we assume the Maxwell model ($\xi = 0$), and take μ and η as variable parameters. Fig. 12 shows the numerical results (the line), which fit the experiments (the circles) relatively well. For silicone oil (Fig. 12a), we use $\mu = 120$ kPa and $\eta = 84$ Pa s. It can be seen that initial rapid shrinkage and following gradual shrinkage with oscillation are reproduced. However, the amplitude of bubble oscillation was too large in the calculation. For syrup (Fig. 12b), we use $\mu = 700$ MPa obtained by the ultrasonic test and $\eta = 1150$ Pa s measured by the rotational viscometer. Agreement of the data and the numerical solution is quite good, and the solution hardly changes if we use $\mu = 960$ MPa obtained by the reflection method.

The rapid oscillation of the bubble in the numerical solution in Fig. 12a occurs in the elastic regime of silicone oil, because the period (~ 0.2 ms) is shorter than the assumed relaxation time ($\eta/\mu = 0.7$ ms). The elastic oscillation is damped as the relaxation time gets shorter and closer to the oscillation period, because a larger fraction of the elastic energy that concerns the oscillation relaxes within a period. The relaxation time is shortened either by increasing the rigidity or decreasing the viscosity. Then, the oscillation amplitudes in the numerical solutions become smaller (Fig. 13a). However, agreement in the general profile becomes poorer. Although the measured rigidity $\mu = 220$ kPa may be available, the oscillation becomes very large and agreement is poor with the measured viscosity $\eta = 960$ Pa s. Thus, we need to assume a much smaller viscosity (Fig. 13b). It may seem contradictory that damping of bubble oscillation increases as the viscosity decreases. Damping usually increases as the viscosity increases in a viscous liquid. However, the oscillation in these figures occurs in the elastic regime, with a period shorter than the relaxation time of the silicone oil. As the viscosity decreases, the relaxation time shortens and becomes closer to the oscillation period. Finally, the elastic energy

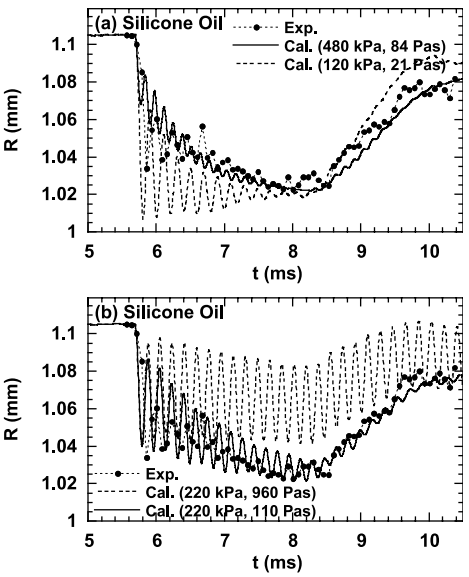

Fig. 13. Numerical solutions for bubble radii with different viscoelastic parameters for the same conditions as in Fig. 12a.

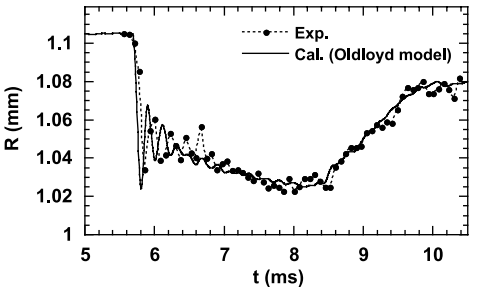

Fig. 14. The numerical solution for bubble radius with the linear Oldroyd model ($\mu = 120$ kPa, $\eta = 84$ Pa s, $\xi = 1.68$ Pa s), which fits the experimental data in the silicone oil.

that concerns the oscillation relaxes within a period and the elastic oscillation vanishes.

Next, the second dashpot of the Oldroyd mode is added. In Fig. 14, we use $\mu = 120$ kPa and $\eta = 84$ Pa s as in Fig. 12, with another viscous component, $\xi = \eta/50$. Agreement between the solution and the experimental data is excellent.

The mechanical properties of the liquids that fit the bubble motion are summarized in Table 1. The relation between these parameters and the measured properties is discussed in Section 6.1.

5.2. Pressure wave in bubbly liquids

We now demonstrate that the different features in the pressure waves can also be ascribed to the different rigidities of the silicone oil and syrup. The same viscoelastic parameters that were used to fit the motion of a single bubble (Table 1) are used in the following calculations. We also included the bulk modulus of the liquid in order to describe wave propagation in the liquid.

A one-dimensional plane pressure wave can be represented in a Fourier integral form as:

$$p(t,z) = \int_{-\infty}^{\infty} F(\omega) e^{i(k_m(\omega)z - \omega t)} d\omega \quad (14)$$

where z is the space axis toward the direction of the wave propagation, t is time, ω is angular frequency, and $F(\omega)$ is the Fourier component of p at $z = 0$. The wave number, $k_m(\omega)$, is given by the dispersion relation for a pressure wave in the bubbly liquid as a function of ω. The mathematical method to obtain the dispersion relation is described in the Appendix.

We assume a stepwise pressure increase at $z = 0$:

$$p(t,0) = \begin{cases} 0 (t \le 0) \\ \Delta p (t > 0) \end{cases} \quad (15)$$

The Fourier transform of Eq. 15 is:

$$F(\omega) = -\frac{\Delta p}{2\pi\omega i} \quad (16)$$

Eq. 16 is substituted into Eq. 14 and the integration in Eq. 14 is partially conducted around the pole at $\omega = 0$. Then one obtains:

$$\frac{p(t,z)}{\Delta p} = \frac{1}{2} - \frac{1}{2\pi i} \int_{+0}^{\infty} \frac{e^{ik_m(\omega)z - i\omega t} - e^{ik_m(-\omega)z + i\omega t}}{\omega} d\omega \quad (17)$$

Eq. 17 is numerically integrated with the trapezoid method. The integration is calculated in the range $10^{-5} \le \omega\overline{R}/c_p \le 1.5$, where $\overline{R}$ is the average bubble radius and c_p is the p-wave velocity of the liquid. These upper and lower bounds were determined so that the step function Eq. 15 was reproduced in the time scale we are interested in ($1\ \mu s < t < 2$ ms). The results of the calculations and experiments are compared in Figs. 15 and 16. The size distributions of the bubbles (frame b) measured in each experiment were used in the calculation. The corresponding dispersion relation

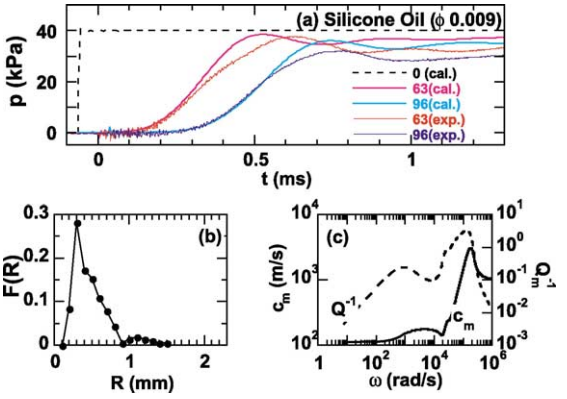

Fig. 15. The pressure wave in silicone oil is calculated using the Oldroyd model with parameters listed in Table 1. The solution is compared with the corresponding experiment in panel a. The measured bubble size distribution (panel b) was used in the calculation. Phase velocity (c_m) and the attenuation factor (Q_m^{-1}) calculated byEqs. A43 and A44 for these conditions are shown in panel c.

(the phase velocity and the attenuation factor) is displayed as a function of frequency in frame c.

In Fig. 15a, the main features of the pressure wave are reproduced by the calculation. Also, the small precursor is recognized in the calculated wave profile. The propagation velocity of the precursor and the main phase in the calculated profile agree well with the experimental data. To obtain complete agreement, we might need two- or three-dimensional calculations including precise positions and sizes of all the bubbles on the wave path (Kameda and Matsumoto, 1996; Kameda et al., 1998).

Agreement of the calculations with the experimental data is not as good for the syrup (Fig. 16) as for the silicone oil. In the experimental data, a small step is separated from the main phase, and the wave front is less steep. Since these characteristics were observed in syrup even without bubbles (Fig. 6), we assume that they are generated by the physical properties of the syrup that have not been represented in the present model, or in the experimental setup. While the pressure is almost constant after the rapid increase at the wave front in the experiment, the calculated pressure continues to increase gradually and becomes much larger than the experimental data. With all these discrepancies unresolved, the calculation represents an important feature: the wave front propagates much faster in syrup than in silicone oil, or than the theoretical velocity given by Eq. 3.

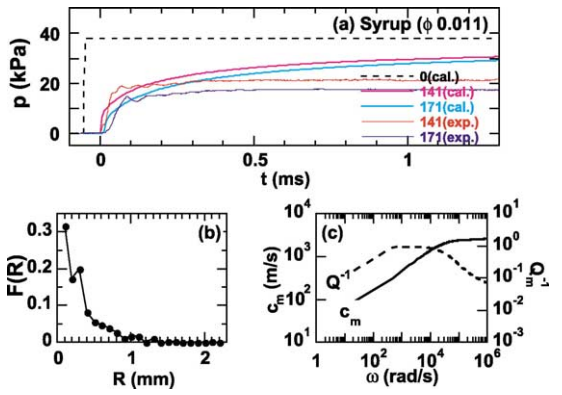

Fig. 16. The pressure wave in syrup is calculated using the Oldroyd model with parameters listed in Table 1. The solution is compared with the corresponding experiment in panel a. The bubble size distributions (panel b) measured in the experiment were used in the calculations. Phase velocity (c_m) and the attenuation factor (Q_m^{-1}) calculated by Eqs. A43 and A44 for these conditions are shown in panel c.

6. Discussion

6.1. Meaning of the fitting parameters

In Section 5.1, we explained the motions of a single bubble in silicone oil and in syrup by employing the linear Oldroyd model. The model includes three parameters, μ, η, and ξ. In syrup, μ and η used in the calculations are consistent with the rigidity and the viscosity measured in the mechanical tests; ξ was not used. On the other hand, in silicone oil, the parameters chosen to fit the numerical solution to the experimental data have not been supported by the mechanical tests. The relation between these parameters and the measured properties of the liquids are discussed below.

The observations of the motion of a single bubble were conducted on a time scale of 0.1–5 ms, bounded by the length of time of the experiment (5 ms) and the frame rate of the video camera ($<13\,500$ fps). If we estimate the relaxation times of the liquids, which are defined by Eq. 11, using the viscosities and the rigidities obtained by the mechanical tests, we obtain 1.2–1.6 μs for the syrup ($\eta=1150$ Pa s, $\mu=700$–980 MPa) and 0.25–4.4 ms for the silicone oil ($\eta=960$ Pa s, $\mu=0.22$–3.9 MPa). The short relaxation time indicates that the syrup is completely in its viscous regime in the experiment. We consider that is why the bubble motion is consistent with the static viscosity. On the other hand, the estimated relaxation time of the silicone oil is exactly in the range of the experiment. Complex liquid behaviors related to viscoelastic properties are expected from this result, and have actually been observed in the experiments.

The dynamic rigidity (μ_ω) corresponding to the model for silicone oil ($\mu=120$ kPa, $\eta=84$ Pa s, $\xi=1.68$ Pa s) was calculated by Eq. A41. The real and the imaginary parts of μ_ω, which are denoted by G' and G'', respectively, are presented by solid

and broken lines in Fig. 9. For comparison, μ_ω was calculated neglecting ξ.

The real part is identical to the previous one, and the imaginary part is presented with a thinner broken line. In the frequency range where $G' > G''$, elastic behavior is dominant, while in the frequency range where $G' < G''$, viscous behavior is dominant (Graessley, 1993). The intersection of the G' and G'' lines, indicated by an arrow, is $\omega = \mu/\eta$, which is the inverse of the relaxation time of the model. The dynamic response of the model is mainly governed by the viscosity η below this frequency, and by the rigidity μ above it. The second viscosity, ξ, starts to influence the results in the higher frequencies.

One might worry about the mismatch between the model and the rheometer test in the low frequencies. It should be noted that the three parameters of the model were determined by the observation of the motion of the bubble in the frequency range indicated in Fig. 9. We consider the model is true in this frequency range, even if it fails in lower frequencies. Actually, we have determined the model parameters from observations of bubble oscillation in lower frequencies (triangles in Fig. 9: data are from Kajitani et al. (2002)). Then, agreement between the model and the rheometer test was better. In many cases, a polymeric liquid has more than one relaxation time. Depending on the time scale, the dynamic response of the liquid may be controlled by different relaxation mechanisms (Graessley, 1993). The behavior of such a liquid is not represented by the three parameters in all the frequency ranges.

The present model introduces the second viscous component ξ to damp high-frequency oscillations. This might represent the viscous damping associated with other relaxation mechanisms that work at higher frequencies. In addition to viscous damping, two other damping mechanisms for bubble oscillation are known: thermal damping due to heat transfer between liquids and the gas in a bubble, and acoustic damping due to the radiation of energy as acoustic waves (Prosperetti, 1991). The thermal damping is effective on the time scale of the thermal diffusion in the bubble, which is estimated with the bubble radius (R_o) and the thermal diffusion coefficient of the gas (κ_g) as R_o^2/κ_g (Prosperetti, 1991). Assuming $R_o = 10^{-3}$ m and $\kappa_g = 10^{-5}$ m^2/s, the time scale is 0.1 s, which is much larger than the period of the oscillation (0.2 ms). We can find few reports discussing acoustic damping in viscoelastic liquids. By analyzing the equation of motion for a bubble in a compressible viscoelastic liquid, which was presented by Brujan (1999), Ichihara et al. (1999) suggested that the acoustic radiation may but partly contribute to damping of the bubble oscillation.

6.2. Implications for bubble dynamics in magma

The experimental and numerical results suggest that behaviors of a single bubble and a liquid–bubble mixture are significantly affected by the viscoelastic properties of the liquid. We now apply the present equations to a magmatic system that takes account of the properties of magma.

There exist a number of studies of viscoelastic properties of silicate melts: ultra-sonics (MHz frequencies) (Macedo et al., 1968; Rivers and Carmichael, 1987; Secco et al., 1991; Webb, 1991), torsion deformation (mHz to Hz) (Mills, 1974; Webb, 1992; Bagdassarov et al., 1993), fiber elongation (mHz) (Li and Uhlmann, 1970; Webb and Dingwell, 1990a,b), viscosity measurements (deformation rates of 10^{-3} s^{-1}) (Li and Uhlmann, 1970; Webb and Dingwell, 1990a,b), and so on. Useful compilations of those data are provided by Bansal and Doremus (1986), Dingwell and Webb (1989), Webb and Dingwell (1995), and Webb (1997). The available data indicate the following features: (1) The composition dependence of the bulk modulus and rigidity in the elastic limit (K and μ, respectively) are relatively small compared with the viscosity. (2) The average value of the rigidity is $\mu = 10^{10\pm0.5}$ (i.e. μ from 3.2 to 32 GPa), and the bulk modulus tends to be a little larger. (3) The viscosity of magma varies by up to 10 orders of magnitude with temperature and composition. The measured viscosity of silicate melts ranges from below 1 to above 10^{14} Pa s. The corresponding relaxation time ranges from 10^{-11} to 10^4 s. (4) Part of the bulk elasticity also relaxes on the same time scale as the rigidity.

Taking account of these features, we represent

K and μ by the fixed values 20 GPa and 10 GPa, respectively, and take the viscosity η as a variable parameter. The density is also represented by a constant: $\rho = 2600$ kg/m^3. The bulk modulus of the bubble, which is equivalent to the pressure, is assumed to be $K_g = 10^6$ Pa. Another viscosity, ξ, and the relaxation associated with the volumetric deformation are neglected. These parameters are summarized in Table 1.

Pressure waves in mixtures of bubbles and magma were calculated with these material constants for various viscosities. The same incident wave, void fraction, and size distribution of bubbles as those in Fig. 16 were assumed. Fig. 17 shows the pressure profiles at a depth of 171 mm, which corresponds to the position of the L2-transducer in the case of Fig. 16. The vertical axis is normalized by the amplitude of the incident shock wave. The following features are noted:

(1) As the viscosity becomes smaller, the propagation velocity approaches the theoretical shock-wave velocity (c_m) given by Eq. 3. As the viscosity becomes larger, it approaches the elastic p-wave velocity (c_p). The theoretical values of these velocities for the present condition are $c_m = 188$ m/s and $c_p = 3580$ m/s, respectively. The estimated arrival times of a wave with velocities of c_m and c_p at a depth of 171 mm are indicated by broken lines in Fig. 17, which are 0.9 and 0.048 ms, respectively.

(2) When the viscosity is small, the pressure wave has a smooth front followed by an oscillation, which is a typical feature of a shock wave in a bubbly liquid with low viscosity. When the viscosity is large, the wave front is as sharp as the incident shock wave.

(3) Attenuation is largest at the intermediate viscosity, where the characteristics of the wave propagation shift from a low-viscosity type to a high-viscosity type.

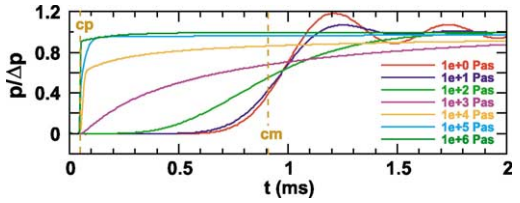

Fig. 17. Pressure waves in the magma with a variety of viscosities are calculated assuming the Oldroyd model with parameters listed in Table 1. The same bubble size distributions and the void fractions as in Fig. 16 are assumed. A stepwise pressure wave penetrates into the magma at 0 ms, and the pressure profiles at a depth of 171 mm are presented.

The calculation presented in Fig. 17 as well as the experimental data suggest that the acoustic properties of bubbly magma are not simply represented by a reduced sound velocity given by Eq. 3 (e.g. Benoit and McNutt, 1997; Garces et al., 1998; Kumagai and Chouet, 2001). To estimate adequate wave velocity and attenuation, we need to take account of the dispersion relation, which significantly depends on liquid rheology. The theoretical dispersion relation also depends on the void fraction, the bubble size distribution, and the pressure. We might need to consider the effects of these parameters for individual conditions, or there might be some simple way to predict wave behavior. In the present paper, we have presented only one numerical result of wave propagation in bubbly magma (Fig. 17) to demonstrate the variation produced by the magma viscosity. More detailed mathematical analyses and parameter studies will be given in a future work.

7. Conclusion

The paper presents experimental results demonstrating the effects of liquid rheology on pressure wave propagation in a liquid–bubble mixture. The experiments were conducted using a high-viscosity silicone oil and a syrup, which have similar static viscosities (1000 Pa s) but different rigidities. From the experimental results and the subsequent numerical analyses, we obtained the following conclusions:

(1) Pressure-wave propagation in a liquid–bubble mixture and motion of a single bubble depend significantly on both the viscosity and the rigidity of the liquid.

(2) Bubbles do not decrease the velocity of pressure waves, when both rigidity and viscosity of the liquid are large. Because magma has a large rigidity, the sound velocity of viscous magma is not decreased by bubbles.

(3) To estimate velocity and attenuation of pressure waves in a viscoelastic liquid with bubbles, we have to take account of the dispersion relation with an adequate viscoelastic model for the liquid. Such a theoretical model has not been completed, and further investigations are required.

(4) Analogous experiments are a useful method to investigate volcanic phenomena. In such experiments, understanding the effects of liquid rheology on bubble dynamics is especially important. The present experiments revealed that quite different phenomena can be observed in liquids with similar viscosities if they have different elasticity.

Acknowledgements

We acknowledge the help of Dr. Y. Takei, Prof. A. Yoneda, and N. Suzuki in the ultrasonic tests, Rheometrics Scientific F.E. Co. in the rheometer tests, and N. Numata, T. Kamemizu, and Y. Nakasato in the shock-tube experiments. We appreciate their collaboration. The present work was supported by the JSPS (Japan Society for the Promotion of Science) and the ACT-JST (Research and Development for Applying Advanced Computational Science and Technology of Japan Science and Technology Corporation).

Appendix A. Acoustic properties of a liquid–bubble mixture

The concept of a mathematical method to calculate the effective bulk modulus, shear modulus, and density of a mixture is as follows. It is supposed that a sinusoidal, plane p-wave is being scattered by a spherical cloud of bubbles in a liquid. When the concentration of the bubbles is small and the interaction between the bubbles is neglected, the scattered wave from the bubble cloud is approximated by $\Sigma_{n=1}^{N}\varphi_n^{sc}$, where φ_n^{sc} is the scattered wave from the nth bubble and N is the total number of bubbles in the cloud. Then a scattered wave from a homogeneous spherical body of the same size as the bubble cloud is considered. The bulk modulus, shear modulus, and density of the body with which the sphere produces the same scattered wave as $\Sigma_{n=1}^{N}\varphi_n^{sc}$ are regarded as representing the effective properties of the liquid–bubble mixture.

This method provides us with mathematical expressions for the effective properties of the mixture using a well-established solution for a scattering problem with a single sphere. The original idea was presented by Kuster and Toksöz (1974) to calculate static moduli of solids or liquids with inclusions. Gaunaurd and Überall (1981) used the same idea to calculate the dynamic bulk modulus of a liquid–bubble mixture. Their formulation includes the effect of resonant oscillation of bubbles, which is a very important factor in such a system. However, it does not include viscosity or shear stress. Combining previous studies, we obtained the effective properties of a mixture of bubbles and viscoelastic liquid.

A.1. Scattering of a p-wave by a single sphere in a viscoelastic liquid

First, we summarize expressions of axially symmetric wave fields in a series of spherical functions (Varadan et al., 1991). Although the following formulations were originally developed for an elastic system, they are applicable to a viscoelastic system by giving the elastic moduli as complex functions of frequency representing the viscoelastic response of the system (Gaunaurd and Überall, 1978).

Let us take a coordinate system (r, θ), where r denotes the radial length and θ denotes the angle with respect to the symmetry axis. Assuming a harmonic wave field with frequency ω, the time dependence of all quantities is suppressed. The scalar potential for a p-wave and the vector potential for an s-wave are:

$$\varphi(\boldsymbol{r}) = \sum_{l=0}^{\infty}(2l+1)\mathrm{i}^{l-1}\frac{A_{\mathrm{p}l}}{k_{\mathrm{p}}}\chi_l(k_{\mathrm{p}}r)P_l(\cos\theta) \qquad \text{(A1)}$$

$$\Psi(\boldsymbol{r}) = \nabla\times\boldsymbol{r}\sum_{l=0}^{\infty}(2l+1)\mathrm{i}^{l-1}\frac{A_{\mathrm{s}l}}{k_{\mathrm{s}}}\chi_l(k_{\mathrm{s}}r)P_l(\cos\theta) \qquad \text{(A2)}$$

where $\boldsymbol{r}$ is the radial vector, $A_{\mathrm{p}l}$ and $A_{\mathrm{s}l}$ are con-

stants particular to the wave field, P_l is the Legendre function, and χ_l is either the spherical Bessel function (j_l) or the spherical Hankel function of the first kind ($h_l^{(1)}$). For the incident plane wave and the wave inside the sphere, which are regular at the origin, j_l is used. For the scattered wave, which propagates outward from the origin, $h_l^{(1)}$ is used. The wave numbers for the p- and s-waves denoted by k_p and k_s are defined as:

$$k_\mathrm{p} = \omega\sqrt{\rho/(K+\frac{4}{3}\mu)},\ k_\mathrm{s} = \omega\sqrt{\rho/\mu} \tag{A3}$$

where K, μ, and ρ are the bulk modulus, the shear modulus (rigidity), and the density of the medium.

The displacement field is:

$$\begin{aligned}\boldsymbol{u}(\boldsymbol{r}) = \nabla\varphi + \nabla\times\Psi = \left(\hat{\boldsymbol{r}}\frac{\partial}{\partial r} + \hat{\boldsymbol{\theta}}\frac{1}{r}\frac{\partial}{\partial\theta}\right)\phi + \\ \left[-\hat{\boldsymbol{r}}\frac{1}{r^2}\left(\frac{\partial^2}{\partial\theta^2} + \frac{1}{\tan\theta}\frac{\partial}{\partial\theta}\right) + \hat{\boldsymbol{\theta}}\frac{1}{r}\frac{\partial^2}{\partial r\partial\theta}\right](r\Psi) \\ = \sum_{l=0}^{\infty}\sum_{\alpha=\mathrm{p,s}}(2l+1)\mathrm{i}^{l-1}A_{\alpha l}\left[\hat{\boldsymbol{r}}U^{\chi}_{r\alpha l}P_l(\cos\theta)\right. \\ \left. +\hat{\boldsymbol{\theta}}\,U^{\chi}_{\theta\alpha l}\frac{\mathrm{d}P_l(\cos\theta)}{\mathrm{d}\theta}\right]\end{aligned} \tag{A4}$$

$$\begin{cases} U^{\chi}_{\mathrm{rp}l} &= [l\chi_l(k_\mathrm{p}r) - k_\mathrm{p}r\chi_{l+1}(k_\mathrm{p}r)]/k_\mathrm{p}r \\ U^{\chi}_{\mathrm{rs}l} &= l(l+1)\chi_l(k_\mathrm{s}r)/k_\mathrm{s}r \\ U^{\chi}_{\theta\mathrm{p}l} &= \chi_l(k_\mathrm{p}r)/k_\mathrm{p}r \\ U^{\chi}_{\theta\mathrm{s}l} &= [(l+1)\chi_l(k_\mathrm{s}r) - k_\mathrm{s}r\chi_{l+1}(k_\mathrm{s}r)]/k_\mathrm{s}r \end{cases} \tag{A5}$$

where $\hat{\boldsymbol{r}}$ and $\hat{\boldsymbol{\theta}}$ are the unit vectors along the r- and θ-axes.

The stress field is:

$$\begin{aligned}\sigma_{rr} = 2\mu\frac{\partial u_r}{\partial r} + \left(K - \frac{2}{3}\mu\right)\nabla\cdot\boldsymbol{u} = \\ \sum_{l=0}^{\infty}\sum_{\alpha=\mathrm{p,s}}(2l+1)\mathrm{i}^{l-1}A_{\alpha l}\frac{S^{\chi}_{rrl}}{r}P_l(\cos\theta)\end{aligned} \tag{A6}$$

$$\begin{aligned}\sigma_{r\theta} = \mu\left[r\frac{\partial}{\partial r}\left(\frac{u_\theta}{r}\right) + \frac{1}{r}\frac{\partial u_r}{\partial\theta}\right] = \\ \sum_{l=0}^{\infty}\sum_{\alpha=\mathrm{p,s}}(2l+1)\mathrm{i}^{l-1}A_{\alpha l}\frac{S^{\chi}_{r\theta\alpha l}}{r}\frac{\mathrm{d}P_l(\cos\theta)}{\mathrm{d}\theta}\end{aligned} \tag{A7}$$

$$\begin{cases} S^{\chi}_{\mathrm{rrp}l} &= 2\mu[l(l-1)\chi_l(k_\mathrm{p}r) + 2k_\mathrm{p}r\chi_{l+1}(k_\mathrm{p}r)]/k_\mathrm{p}r - \rho\omega^2r^2\chi_l(k_\mathrm{p}r)/k_\mathrm{p}r \\ S^{\chi}_{\mathrm{rrs}l} &= 2\mu l(l+1)[(l-1)\chi_l(k_\mathrm{s}r) - k_\mathrm{s}r\chi_{l+1}(k_\mathrm{s}r)]/k_\mathrm{s}r \\ S^{\chi}_{r\theta\mathrm{p}l} &= 2\mu[(l-1)\chi_l(k_\mathrm{p}r) - k_\mathrm{p}r\chi_{l+1}(k_\mathrm{p}r)]/k_\mathrm{p}r \\ S^{\chi}_{r\theta\mathrm{s}l} &= 2\mu[(l^2-1)\chi_l(k_\mathrm{s}r) + k_\mathrm{s}r\chi_{l+1}(k_\mathrm{s}r)]/k_\mathrm{s}r - \rho\omega^2r^2\chi_l(k_\mathrm{s}r)/k_\mathrm{s}r \end{cases} \tag{A8}$$

Next we specify $A_{\mathrm{p}l}$ and $A_{\mathrm{s}l}$ for the scattered wave from a single sphere in an infinite body of viscoelastic liquid. The radius of the sphere is denoted by a.

The displacement field outside the sphere is:

$$\begin{aligned}\boldsymbol{u}(\boldsymbol{r}) = \hat{\boldsymbol{z}}\exp(\mathrm{i}k_\mathrm{p}z) + \boldsymbol{u}^{\mathrm{sc}}(\boldsymbol{r}) = \\ \nabla\varphi^{\mathrm{inc}} + \nabla\varphi^{\mathrm{sc}} + \nabla\times\Psi^{\mathrm{sc}}\end{aligned} \tag{A9}$$

where $\hat{\boldsymbol{z}}$ is a unit vector pointing in the direction of the incident p-wave ($\theta = 0$), and the incident and scattered waves are denoted with superscripts 'inc' and 'sc', respectively. According to Eqs. A1 and A2, these potentials are expressed in terms of spherical functions as:

$$\varphi^{\mathrm{inc}}(\boldsymbol{r}) = \sum_{l=0}^{\infty}(2l+1)\mathrm{i}^{l-1}\frac{1}{k_\mathrm{p}}j_l(k_\mathrm{p}r)P_l(\cos\theta) \tag{A10}$$

$$\varphi^{\mathrm{sc}}(\boldsymbol{r}) = \sum_{l=0}^{\infty}(2l+1)\mathrm{i}^{l-1}\frac{A_{\mathrm{p}l}}{k_\mathrm{p}}h_l^{(1)}(k_\mathrm{p}r)P_l(\cos\theta) \tag{A11}$$

$$\begin{aligned}\Psi^{\mathrm{sc}}(\boldsymbol{r}) = \\ \nabla\times\boldsymbol{r}\sum_{l=0}^{\infty}(2l+1)\mathrm{i}^{l-1}\frac{A_{\mathrm{s}l}}{k_\mathrm{s}}h_l^{(1)}(k_\mathrm{s}r)P_l(\cos\theta)\end{aligned} \tag{A12}$$

Let us denote all the quantities related to the material inside the sphere with $\tilde{}$. The wave field inside the sphere is represented in the same way as:

$$\tilde{\boldsymbol{u}}(\boldsymbol{r}) = \nabla\tilde{\varphi} + \nabla\times\tilde{\Psi} \tag{A13}$$

$$\tilde{\varphi}(\boldsymbol{r}) = \sum_{l=0}^{\infty}(2l+1)\mathrm{i}^{l-1}\frac{\tilde{A}_{\mathrm{p}l}}{\tilde{k}_\mathrm{p}}j_l(\tilde{k}_\mathrm{p}r)P_l(\cos\theta) \tag{A14}$$

$$\tilde{\Psi}(\boldsymbol{r}) = \nabla\times\boldsymbol{r}\sum_{l=0}^{\infty}(2l+1)\mathrm{i}^{l-1}\frac{\tilde{A}_{\mathrm{s}l}}{\tilde{k}_\mathrm{s}}j_l(\tilde{k}_\mathrm{s}r)P_l(\cos\theta) \tag{A15}$$

At the surface of the sphere ($r = a$), displacement and the stress are continuous, so that:

$$\begin{pmatrix} U^{h(1)}_{\mathrm{rp}0} & -\tilde{U}^{j}_{\mathrm{rp}0} \\ S^{h(1)}_{\mathrm{rrp}0} & -\tilde{S}^{j}_{\mathrm{rrp}0} \end{pmatrix}\begin{pmatrix} A_{\mathrm{p}0} \\ \tilde{A}_{\mathrm{p}0} \end{pmatrix} = \begin{pmatrix} -U^{j}_{\mathrm{rp}0} \\ -S^{j}_{\mathrm{rrp}0} \end{pmatrix} \tag{A16}$$

$$\begin{pmatrix} U^{h(1)}_{rpl} & U^{h(1)}_{rsl} & -\tilde{U}^{j}_{rpl} & -\tilde{U}^{j}_{rsl} \\ U^{h(1)}_{\theta pl} & U^{h(1)}_{\theta sl} & -\tilde{U}^{j}_{\theta pl} & -\tilde{U}^{j}_{\theta sl} \\ S^{h(1)}_{rrpl} & S^{h(1)}_{rrsl} & -\tilde{S}^{j}_{rrpl} & -\tilde{S}^{j}_{rrsl} \\ S^{h(1)}_{r\theta pl} & S^{h(1)}_{r\theta sl} & -\tilde{S}^{j}_{r\theta pl} & -\tilde{S}^{j}_{r\theta sl} \end{pmatrix} \begin{pmatrix} A_{pl} \\ A_{sl} \\ \tilde{A}_{pl} \\ \tilde{A}_{sl} \end{pmatrix} = \begin{pmatrix} -U^{j}_{rpl} \\ -U^{j}_{\theta pl} \\ -S^{j}_{rrpl} \\ S^{j}_{r\theta pl} \end{pmatrix} (l \geq 1) \tag{A17}$$

where U and S are defined in Eqs. A5 and A8.

Using the long-wave approximation, $|k_\alpha|a \ll 1$, $|\tilde{k}_\alpha|a \ll 1$ (α = p,s), only the terms of the lowest degree in frequency are retained in Eqs. A16 and A17. For $l = 0$, 1, 2, one obtains (Korneev and Johnson, 1993):

$$A_{p0} = -i\frac{(k_p a)^3}{3}\frac{\tilde{K}-K}{\tilde{K}+\frac{4}{3}\mu} \tag{A18}$$

$$A_{p1} = i\frac{(k_p a)^3}{9}\left(\frac{\tilde{\rho}}{\rho}-1\right) \tag{A19}$$

$$A_{p2} = -i\frac{4(k_p a)^3\varepsilon^2}{45}\left(\frac{\tilde{\mu}}{\mu}-1\right)[1+ \frac{2}{15}\left(\frac{\tilde{\mu}}{\mu}-1\right)(3+2\varepsilon^2)]^{-1} \tag{A20}$$

$$A_{s0} = 0 \tag{A21}$$

$$A_{s1} = \frac{A_{p1}}{\varepsilon^3} \tag{A22}$$

$$A_{s2} = \frac{1}{2}\frac{A_{p2}}{\varepsilon^4} \tag{A23}$$

where

$$\varepsilon = \frac{k_p}{k_s} = \sqrt{\frac{\mu}{K+\frac{4}{3}\mu}} \tag{A24}$$

Eqs. A18–A20 are equivalent to equation 17 of Korneev and Johnson (1993). The coefficients a_l and b_l in their paper correspond to $-A_{pl}$ and A_{sl}, respectively.

The above formulation does not include the resonance of the sphere. In many cases, the resonances of inclusions are located at relatively large frequencies. However, in cases of a bubble in viscous or viscoelastic liquids with no or a very small rigidity, the monopole resonance ($l = 0$) occurs in the low-frequency region (Gaunaurd and Überall, 1981). They noticed that the term $\rho\omega^2 a^2$, which is a higher-order term with respect to frequency, is larger than the other lower-order terms, when ρ is much larger than either of μ, $\tilde{\mu}$, and $\tilde{\rho}$. Leaving the term in the long-wave approximation, one obtains:

$$A_{p0} = -i\frac{(k_p a)^3}{3}\frac{\tilde{K}-K}{\tilde{K}+\frac{4}{3}\mu-\frac{1}{3}\rho\,\omega^2 a^2(1+ik_p a)} \tag{A25}$$

The frequencies of higher resonant modes are beyond the range of the long-wave approximation and are negligible (Gaunaurud and Überall, 1981).

Eqs. A19 and A20 are obtained using the long-wave approximation for both p- and s-waves. However, when the material is gas, or liquid as in the present case, the s-wave is absent or its wavelength may be much shorter than that of the p-wave. Therefore, it is necessary to check if these expressions are applicable to fluids with $\mu = 0$ and/or $\mu = 0$.

In the case that only the internal material is fluid ($\mu = 0$, $\mu \neq 0$), Eq. A17 becomes:

$$\begin{pmatrix} U^{h(1)}_{rpl} & U^{h(1)}_{rsl} & -\tilde{U}^{j}_{rpl} \\ S^{h(1)}_{rrpl} & S^{h(1)}_{rrsl} & -\tilde{S}^{j}_{rrpl} \\ S^{h(1)}_{r\theta pl} & S^{h(1)}_{r\theta sl} & 0 \end{pmatrix} \begin{pmatrix} A_{pl} \\ A_{sl} \\ \tilde{A}_{pl} \end{pmatrix} = \begin{pmatrix} -U^{j}_{rpl} \\ -S^{j}_{rrpl} \\ -S^{j}_{r\theta pl} \end{pmatrix} \tag{A26}$$

The corresponding solutions are:

$$A_{p1} = i\frac{(k_p a)^3}{9}\left(\frac{\tilde{\rho}}{\rho}-1\right) \tag{A27}$$

$$A_{p2} = i\frac{4(k_p a)^3}{3}\frac{\varepsilon^2}{9-4\varepsilon^2} \tag{A28}$$

These equations agree with Eqs. A19 and A20 with $\tilde{\mu} = 0$.

In the case that both the internal and the external materials are fluid ($\tilde{\mu} = \mu = 0$), we have

$$\begin{pmatrix} U^{h(1)}_{rpl} & -\tilde{U}^{j}_{rpl} \\ S^{h(1)}_{rrpl} & -\tilde{S}^{j}_{rrpl} \end{pmatrix} \begin{pmatrix} A_{pl} \\ \tilde{A}_{pl} \end{pmatrix} = \begin{pmatrix} -U^{j}_{rpl} \\ -S^{j}_{rrpl} \end{pmatrix} \tag{A29}$$

$$A_{pl} = -i\frac{(k_p a)^3}{3}\frac{\rho-\tilde{\rho}}{\rho+2\tilde{\rho}} \tag{A30}$$

$$A_{p2} = 0 \tag{A31}$$

Eq. A31 agrees with Eq. A20 with $\mu = 0$ ($k_s \to \infty$), while Eq. A30 does not agree with Eq. A19. Therefore, we have to choose Eq. A19 when the external material is closer to a solid ($|\mu| \sim |K|$), and Eq. A30 when it is closer to a fluid ($|\mu| \ll |K|$).

A.2. Effective properties of a viscoelastic liquid containing bubbles

Let us assume N bubbles in a spherical region of radius R_c in an infinite body of liquid. The origin of the coordinate is taken at the center of the sphere. When we neglect interaction between the bubbles, the p-wave scattered from the region containing bubbles is represented by:

$$\varphi^{sc}(\boldsymbol{r}) = \sum_{n=1}^{N} \varphi_n^{sc}(\boldsymbol{r} - \boldsymbol{r}_n) \tag{A32}$$

where $\varphi_n^{sc}(\boldsymbol{r}-\boldsymbol{r}_n)$ is the p-wave potential scattered by a single bubble at $\boldsymbol{r}_n$. At a large distance from the bubbles, we may approximate $\boldsymbol{r}-\boldsymbol{r}_n \sim \boldsymbol{r}$, and

$$\varphi^{sc}(\boldsymbol{r}) = \sum_{n=1}^{N}\sum_{l=0}^{\infty}(2l+1)\mathrm{i}^{l-1}\frac{A^n_{pl}}{k_p}h_l^{(1)}(k_p r)P_l(\cos\theta) \tag{A33}$$

The bulk modulus and the density of the gas in the bubbles are represented by K_g and ρ_g, respectively. The bulk modulus and rigidity of the viscoelastic liquid are denoted as K_ω and μ_ω, respectively, which are complex functions of frequency. The density of the liquid is ρ. Then $A^n{}_{p0,1,2}$ in Eq. A33 is obtained from Eqs. A25, A19 (or A30), and A20 with $(K,\ \mu,\ \rho) = (K_\omega,\ \mu_\omega,\ \rho)$, $(\tilde{K},\ \tilde{\mu},\ \tilde{\rho}) = (K_g,\ 0,\ \rho_g)$, and $a = R_n$, where R_n is the radius of the nth bubble.

On the other hand, a cloud of bubbles is regarded as a homogeneous sphere of the same size with bulk modulus K_m, shear modulus μ_m, and density ρ_m. The radius of the sphere, R_c, is assumed to be small enough so that a long-wave approximation is applicable for the assumed incident wave, and that the frequency of the resonance of the sphere lies above the limit of validity of the low-frequency expansion, while it is assumed to be large enough to include many bubbles. Gaunaurd and Überall (1981) assumed its radius about 20 times as large as those of the bubbles. In this case, the scattered wave from the sphere, $\varphi^{sc}(r)$:

$$\varphi^{sc}(\boldsymbol{r}) = \sum_{l=0}^{\infty}(2l+1)\mathrm{i}^{l-1}\frac{A^m_{pl}}{k_p}h_l^{(1)}(k_p r)P_l(\cos\theta) \tag{A34}$$

where $A^m_{p0,1,2}$ are given by Eq. A18, which is the one without resonance, Eq. A19 (or A30), and Eq. A20 with substitution of $(K,\ \mu,\ \rho) = (K_\omega,\ \mu_\omega,\ \rho)$, $(\tilde{K},\ \tilde{\mu},\ \tilde{\rho}) = (K_m,\ \mu_m,\ \rho_m)$, and $a = R_c$.

In order that Eqs. A33 and A34 agree with each other:

$$A^m_{pl} = \sum_{n=1}^{N} A^n_{pl}\ (l = 0, 1, 2, \ldots) \tag{A35}$$

We represent the number fraction of the bubbles with radius R by $f(R)$ and replace $\Sigma_{n=1}^{N}$ by $N\int_0^\infty f(R)\mathrm{d}R$. Using Eq. A35 for $l = 0$, 1, 2, we obtain K_m, μ_m, and ρ_m as:

$$K_m = \frac{K_\omega + \frac{4}{3}\phi\Gamma\mu_\omega}{1-\phi\Gamma} \tag{A36}$$

with:

$$\Gamma = \frac{K_g - K_\omega}{K_g + \frac{4}{3}\mu_\omega} \times \frac{\int_0^\infty f(R)\dfrac{R^3}{1-\dfrac{\rho\omega^2R^2}{3K_g+4\mu_\omega}\left(1+\mathrm{i}\omega R\sqrt{\dfrac{\rho}{K_\omega+\frac{4}{3}\mu_\omega}}\right)}\mathrm{d}R}{\int_0^\infty f(R)R^3\mathrm{d}R}$$

and:

$$\mu_m = \mu_\omega\left[1 - \frac{\phi}{1-\dfrac{2}{15}(1-\phi)\left(3+\dfrac{2\mu_\omega}{K_\omega+\frac{4}{3}\mu_\omega}\right)}\right] \tag{A37}$$

$$\rho_m = \rho_g\phi + \rho(1-\phi)\ (|\mu_\omega| \sim |K_\omega|) \tag{A38}$$

$$\rho_m = \rho \frac{1-\phi(\rho-\rho_g)/(\rho+2\rho_g)}{1+2\phi(\rho-\rho_g)/(\rho+2\rho_g)} (|\mu_\omega| \ll |K_\omega|) \quad \text{(A39)}$$

where $\phi = \Sigma_{n=1}^{N} R_n^3/R_c^3 = N\int_0^\infty f(R)R^3 dR/R_c^3$ is the void fraction. It is noted that the effective bulk modulus has a complicated form, including not only the bulk modulus and the void fraction, but also the rigidity of the liquid and the resonance of the bubbles. On the other hand, the effective rigidity and density are mainly determined by the liquid property, with small modifications proportional to the void fraction. The effective density depends on the void fraction in different ways in cases that the matrix is close to a solid ($|\mu_\omega| \sim |K_\omega|$) and to fluid ($|\mu_\omega| \ll |K_\omega|$) In the case of a fluid matrix, where relative motion between the inclusion and matrix can occur, the effective density Eq. A39 is governed by inertia and is different from Eq. A38, which is governed by gravity (Kuster and Toksöz, 1974).

A.3. A constitutive model for the viscoelastic liquid

We assume the linear Oldroyd model represents the shear rheology of the liquid. Viscoelasticity associated with volumetric deformation is neglected and $K_\omega = K$ (constant) is assumed. The differential equation representing the stress–strain relation for the linear Oldroyd model (Fig. 11) is:

$$\sigma + \frac{\eta}{\mu}\frac{d\sigma}{dt} = (\eta+\xi)\frac{d\varepsilon}{dt} + \frac{\eta\xi}{\mu}\frac{d^2\varepsilon}{dt^2} \quad \text{(A40)}$$

where σ is the shear stress and ε is the shear strain (Fogler and Goddard, 1971). When we assume a periodic field as $\sigma = \sigma_\omega e^{i\omega t}$ and $\varepsilon = \varepsilon_\omega e^{i\omega t}$, and define the complex dynamic rigidity μ_ω, Eq. A40 is rewritten as:

$$\sigma = \mu_\omega \varepsilon_\omega = \frac{i\omega(\eta+\xi) - \omega^2 \frac{\eta\xi}{\mu}}{1 + i\omega\frac{\eta}{\mu}} \varepsilon_\omega \quad \text{(A41)}$$

The dispersion relation for the pressure wave in the mixture is given in the same way as in an elastic medium by:

$$\frac{\omega^2}{k_m(\omega)^2} = \frac{K_m(\omega) + \frac{4}{3}\mu_m(\omega)}{\rho_m} \quad \text{(A42)}$$

$$c_m(\omega) = \frac{\omega}{\mathrm{Re}\, k_m(\omega)} \quad \text{(A43)}$$

$$Q_m^{-1} = \frac{\mathrm{Im}\, k_m(\omega)}{\mathrm{Re}\, k_m(\omega)} \quad \text{(A44)}$$

where $k_m(\omega)$ is the wave number, c_m is the phase velocity, and Q_m^{-1} is the attenuation factor (Gaunaurd and Überall, 1981).

References

Bagdassarov, N.S., Dingwell, D.B., 1993. Frequency dependent rheology of vesicular rhyolite. J. Geophys. Res. 98, 6477–6487.

Bagdassarov, N.S., Dingwell, D.B., Webb, S.L., 1993. Effect of boron phosphorus and fluorine on shear stress relaxation in haplogranitic melt. Eur. J. Mineral. 5, 409–425.

Bansal, N.P., Doremus, R.H., 1986. Handbook of Glass Properties. Academic Press, New York, pp. 680.

Barnes, H.A., Hutton, J.F., Walters, K., 1989. An Introduction to Rheology. Elsevier, pp. 37–43.

Benoit, J.P., McNutt, S.R., 1997. New constraints on source processes of volcanic tremor at Arenal volcano, Costa Rica, using broadband seismic data. Geophys. Res. Lett. 24, 449–452.

Brujan, E.A., 1999. A first-order model for bubble dynamics in a compressible viscoelastic liquid. J. Non-Newtonian Fluid Mech. 84, 83–103.

Brujan, E.A., Ohl, C.-D., Lauterborn, W., Philipp, A., 1996. Dynamics of laser-induced cavitation bubbles in polymer solutions. ACUSTICA 82, 423–430.

Caflish, R.E., Miksis, M.J., Papanicolaou, G.C., Ting, L., 1985. Effective equation for wave propagation in bubbly liquids. J. Fluid Mech. 153, 259–273.

Campbell, I.J., Pitcher, A.S., 1958. Shock waves in a liquid containing gas bubbles. Proc. R. Soc. London A 243, 534–545.

Cheyne, S.A., Stebbings, C.T., Roy, R.A., 1995. Phase velocity measurements in bubbly liquids using a fiber optic laser interferometer. J. Acoust. Soc. Am. 97, 1621–1624.

Chouet, B.A., 1996. New methods and future trends in seismological volcano monitoring. In: Monitoring and Mitigation of Volcano Hazards. Springer, Berlin, pp. 23–97.

Commander, K.W., Prosperetti, A., 1989. Linear pressure waves in bubbly liquids: Comparison between theory and experiments. J. Acoust. Soc. Am. 85, 732–746.

Dingwell, D.B., Webb, S.L., 1989. Structural relaxation in silicate melts and non-newtonian melt rheology in geologic processes. Phys. Chem. Miner. 16, 508–516.

Fogler, H.S., Goddard, J.D., 1970. Collapse of spherical cavities in viscoelastic fluids. Phys. Fluids 13, 1135–1141.

Fogler, H.S., Goddard, J.D., 1971. Oscillations of a gas bubble in viscoelastic liquids subject to acoustic and impulsive pressure variations. J. Appl. Phys. 42, 259–263.

Garces, M.A., McNutt, S.R., 1997. Theory of the sound field generated by a resonant magma conduit. J. Volcanol. Geotherm. Res. 78, 155–178.

Garces, M.A., Hagerty, M.T., Schwartz, S.Y., 1998. Magma acoustics and time-varying melt properties at Arenal Volcano, Costa Rica. Geophys. Res. Lett. 25, 2293–2296.

Garces, M.A., McNutt, S.R., Hansen, R.A., Eichelberger, J.C., 2000. Application of wave-theoretical seismoacoustic models to the interpretation of explosion and eruption tremor signals radiated by Pavlof volcano, Alaska. J. Geophys. Res. 105, 3039–3058.

Gaunaurd, G.C., Überall, H., 1978. Theory of resonant scattering from spherical cavities in elastic and viscoelastic media. J. Acoust. Soc. Am. 63, 1699–1712.

Gaunaurd, G.C., Überall, H., 1981. Resonance theory of bubbly liquids. J. Acoust. Soc. Am. 69, 362–370.

Graessley, W.W., 1993. Viscoelasticity and flow in polymer melts and concentrated solutions. In: Mark, J.E., Eisenberg, A., Graessley, W.W., Mandelkern, L., Samulski, E.T., Koenig, J.L., Wignall, G.D. (Eds.), Physical Properties of Polymers, 2nd edn. Am. Chem. Soc. pp. 97–143.

Ichihara, M., Ohkunitani, H., Kameda, M., 1999. Bubble oscillation in a compressible viscoelastic liquid: Theory and experiment. Proc. ASME/JSME FEDSM'99, p. 6766.

Kajitani, M., Kamemizu, T., Kameda, M., Ichihara, M., 2002. Dynamic viscoelasticity parameter measurement using the bubble oscillation. Proc. Mech. Eng. Congress 3, pp. 15–16 (in Japanese with English abstract).

Kameda, M., Matsumoto, Y., 1996. Shock waves in a liquid containing small gas bubbles. Phys. Fluids 8, 322–335.

Kameda, M., Matsumoto, Y., 1999. Nonlinear oscillation of a spherical gas bubble in acoustic fields. J. Acoust. Soc. Am. 106, 3156–3166.

Kameda, M., Shimaura, N., Higashino, F., Matsumoto, Y., 1998. Shock waves in a uniform bubbly flow. Phys. Fluids 10, 2661–2668.

Keller, J.B., Miksis, M.J., 1980. Bubble oscillations of large amplitude. J. Acoust. Soc. Am. 68, 628–633.

Kiefer, S.W., 1977. Sound speed in liquid-gas mixtures: water-air and water-steam. J. Geophys. Res. 82, 2895–2904.

Korneev, V.A., Johnson, L.R., 1993. Scattering of elastic waves by a spherical inclusion-II. Limitations of asymptotic solutions. Geophys. J. Int. 115, 251–263.

Kumagai, H., Chouet, B., 2001. The dependence of acoustic properties of a crack on the resonance mode and geometry. Geophys. Res. Lett. 28, 3325–3328.

Kuster, G.T., Toksöz, M.N., 1974. Volocity and attenuation of seismic waves in two-phase media: 1. Theoretical formulations. Geophysics 39, 587–606.

Lane, S.J., Chouet, B.A., Phillips, J.C., Dawson, P., Ryan, G.A., Hurst, E., 2001. Experimental observations of pressure oscillations and flow regimes in an analogue volcanic system. J. Geophys. Res. 106, 6461–6476.

Li, J.H., Uhlmann, D.R., 1970. The flow of glass at high stress levels I. Non-Newtonian behavior of homogeneous $0.08Rb_2O$ $0.92SiO_2$ glasses. J. Non-Cryst. Solids 3, 127–147.

Llewellin, E.W., Mader, H.M., Wilson, S.D.R., 2002. The rheology of a bubbly liquid. Proc. R. Soc. London A 458, 987–1016.

Macedo, P.B., Simmons, J.H., Haller, W., 1968. Spectrum of relaxation times and fluctuation theory: ultrasonic studies on an alkali-borosillicate melt. Phys. Chem. Glasses 9, 156–164.

Manga, M., Loewenberg, M., 2001. Viscosity of magmas containing highly deformable bubbles. J. Volcanol. Geotherm. Res. 105, 19–24.

Matsumoto, Y., Kameda, M., 1996. Propagation of shock waves in dilute bubbly liquids (Governing equations, Hugoniot relations, and effect of slippage between two phases). JSME Int. J. Ser. B 39, 264–272.

Matsuo, K., Aoki, T., Miyazato, Y., Handa, T., Oka, H., Kobayashi, M., 1997. Characteristics of pressure wave propagation through bubbly flow in a vertical pipe. Proc. 16th Multiphase Flow Symposium, Japan, pp. 131–134 (in Japanese).

Mikada, M., 1992. Volcanic tremor originating from Asama Volcano: Interpretation of tremor associated with the 1973 and the 1982 activity (in Japanese). Bull. Volcanol. Soc. Jpn. 37, 21–33.

Mills, J.J., 1974. Low frequency storage and loss moduli of soda silica glasses in the transformation range. J. Non-Cryst. Solids 14, 225–268.

Nishimura, T., Chouet, B., 2002. Numerical simulation of the seismic waves and compressible fluid motions associated with volcanic eruptions. Abstract of 2002 Joint Meeting, Earth Planet. Sci., Japan, V072-002.

Noordzij, L., van Wijngaarden, L., 1974. Relaxation effects, caused by relative motion, on shock waves in gas-bubble/liquid mixtures. J. Fluid Mech. 66, 115–143.

Phillips, J.C., Lane, S.J., Lejeune, A.M., Hilton, M., 1995. Gum rosin-acetone system as an analogue to the degassing behavior of hydrated magmas. Bull. Volcanol. 57, 263–268.

Prosperetti, A., 1984. Bubble phenomena in sound fields 2. Ultrasonics 22, 115–124.

Prosperetti, A., 1991. The thermal behavior of oscillating gas bubbles. J. Fluid Mech. 222, 587–616.

Prosperetti, A., Lezzi, A., 1986. Bubble dynamics in a compressible liquid. Part 1. First-order theory. J. Fluid Mech. 168, 457–478.

Rayleigh, L., 1917. On the pressure developed in a liquid during the collapse of a spherical cavity. Phil. Mag. 6th Ser. 34, 94–98.

Ripepe, M., Gordeev, E., 1999. Gas bubble dynamics model for shallow volcanic tremor at Stromboli. J. Geophys. Res. 104, 10639–10654.

Ripepe, M., Poggi, P., Braun, T., Gordeev, E., 1996. Infrasonic waves and volcanic tremor at Stromboli. Geophys. Res. Lett. 23, 181–184.

Rivers, M.L., Carmichael, I.S.E., 1987. Ultrasonic studies of silicate melts. J. Geophys. Res. 92, 9247–9270.

Secco, R.A., Manghnani, M.H., Liu, T.-C., 1991. The bulk modulus-attenuation-viscosity systematics of diopside-anorthite melts. Geophys. Res. Lett. 18, 93–96.

Shima, A., 1997. Studies on bubble dynamics. Shock Waves 7, 33–42.

Silberman, E., 1957. Sound velocity and attenuation in bubbly mixtures measured in standing wave tubes. J. Acoust. Soc. Am. 29, 925–933.

Takemura, F., Matsumoto, Y., 1994. Influence of internal phenomena on gas bubble motion (Effects of transport phenomena and mist formation inside bubble in the expanding phase). JSME Int. J. Ser. B 37, 736–745.

Tanasawa, I., Yang, W.-J., 1970. Dynamic behavior of a gas bubble in viscoelastic liquids. J. Appl. Phys. 41, 4522–4531.

van Wijngaarden, L., 1972. One-dimensional flow of liquids containing small gas bubbles. Annu. Rev. Fluid Mech. 4, 369–396.

Varadan, V.K., Varadan, V.V., Ma, Y., 1985. A propagator model for scattering of acoustic waves by bubbles in water. J. Acoust. Soc. Am. 78, 1879–1881.

Varadan, V.V., Ma, Y., Varadan, V.K., Lakhtakia, A., 1991. Scattering of waves by spheres and cylinders. In: Varadan, V.V., Lakhtakia, A., Varadan, V.K. (Eds.), Field Representations and Introduction to Scattering. Elsevier/North Holland, pp. 211–324.

Vergniolle, S., Brandeis, G., 1994. Origin of the sound generated by Strombolian explosions. Geophys. Res. Lett. 21, 1959–1962.

Vergniolle, S., Brandeis, G., 1996. Strombolian explosions 1. A large bubble breaking at the surface of a lava column as a source of sound. J. Geophys. Res. 101, 20433–20447.

Webb, S.L., 1991. Shear and volume relaxation in $Na_2Si_2O_5$. Am. Mineral. 76, 1449–1454.

Webb, S.L., 1992. Low-frequency shear and structural relaxation in rhyolite melt. Phys. Chem. Mineral. 19, 240–245.

Webb, S.L., 1997. Silicate melts: Relaxation, rheology, and glass transition. Rev. Geophys. 35, 191–218.

Webb, S.L., Dingwell, D.B., 1990a. The onset of non-Newtonian rheology of silicate melts: A fiber elongation study. Phys. Chem. Mineral. 17, 125–132.

Webb, S.L., Dingwell, D.B., 1990b. Non-Newtonian rheology of igneous melts at high stresses and strain rates: Experimental results for rhyolite, andesite, basalt, and nephelinite. Geophys. Res. 95, 15695–15701.

Webb, S.L., Dingwell, D.B., 1995. Viscoelasticity. In: Stebbins, J.F., McMillan, P.F., Dingwell, D.B. (Eds.), Structure, Dynamics, and Properties of Silicate Melts. Rev. Mineral. 32, pp. 95–119.

Yoneda, A., 1998. Liquid-solid hybrid resonance method for investigating acoustic properties of magmas. In: Nakahara, M., Eds Rev. High Pressure Sci. Technol., Japan Soc. High Pressure Sci. and Tech., Kyoto, Japan, pp. 79–82.

Yoneda, A., 2000. The xyzr algorithm specialized for eigenvibration problem of bored and laminated objects. J. Sound Vib. 236, 431–441.

Zimanowski, B., Fröhlich, Lorenz, V., 1991. Quantitative experiments on phreatomagmatic explosions. J. Volcanol. Geotherm. Res. 48, 341–358.